

## THE ELIXR GALAXY SURVEY. II: BARYONS AND DARK MATTER IN AN ISOLATED ELLIPTICAL GALAXY

PHILIP J. HUMPHREY<sup>1</sup>, DAVID A. BUOTE<sup>1</sup>, EWAN O’SULLIVAN<sup>2,3</sup>, AND TREVOR J. PONMAN<sup>3</sup>

*Draft version November 7, 2018*

### ABSTRACT

The Elliptical Isolated X-ray (ELIXr) Galaxy Survey is a volume-limited ( $< 110\text{Mpc}$ ) study of optically selected, isolated,  $L_*$  elliptical galaxies, to provide an X-ray census of galaxy-scale (virial mass,  $M_{\text{vir}} \lesssim 10^{13} M_{\odot}$ ) objects, and identify candidates for detailed hydrostatic mass modelling. In this paper, we present a *Chandra* and *XMM* study of one such candidate, NGC 1521, and constrain its distribution of dark and baryonic matter. We find a morphologically relaxed hot gas halo, extending almost to  $R_{500}$ , that is well described by hydrostatic models similar to the benchmark, baryonically closed, Milky Way-mass elliptical galaxy NGC 720. We obtain good constraints on the enclosed gravitating mass ( $M_{500} = [3.8 \pm 1.0] \times 10^{12} M_{\odot}$ , slightly higher than NGC 720), and baryon fraction ( $f_{b,500} = 0.13 \pm 0.03$ ). We confirm at  $8.2\text{-}\sigma$  the presence of a dark matter (DM) halo consistent with  $\Lambda\text{CDM}$ . Assuming a Navarro-Frenk-White DM profile, our self-consistent, physical model enables meaningful constraints beyond  $R_{500}$ , revealing that most of the baryons are in the hot gas. Within the virial radius,  $f_b$  is consistent with the Cosmic mean, suggesting that the predicted massive, quasi-hydrostatic gas halos may be more common than previously thought. We confirm that the DM and stars conspire to produce an approximately powerlaw total mass profile ( $\rho_{\text{tot}} \propto r^{-\alpha}$ ) that follows the recently discovered scaling relation between  $\alpha$  and optical effective radius. Our conclusions are insensitive to modest, observationally motivated, deviations from hydrostatic equilibrium. Finally, after correcting for the enclosed gas fraction, the entropy profile is close to the self-similar prediction of gravitational structure formation simulations, as observed in massive galaxy clusters.

*Subject headings:* dark matter— Xrays: galaxies— galaxies: elliptical and lenticular, cD— galaxies: ISM— galaxies: formation — galaxies: individual (NGC1521) — galaxies: fundamental parameters

### 1. INTRODUCTION

The distribution of mass in galaxies, both in the form of baryons and dark matter (DM), is a crucial yardstick for elucidating galaxy formation and evolution. Dissipationless DM simulations in our current ( $\Lambda\text{CDM}$ ) cosmological paradigm predict DM halos with a characteristic density profile (Navarro et al. 1997, 2004), the average shape of which varies slowly with mass (Bullock et al. 2001; Macciò et al. 2008). In the centres of these halos, baryons condense into stars, but the complex interplay of gas cooling and heating involved (including accretion shocks, feedback from supernovae, stellar winds, and active galactic nuclei) has been the subject of vigorous debate (e.g. White & Rees 1978; White & Frenk 1991; Kereš et al. 2005; Hopkins et al. 2006; Croton et al. 2006). Current models tend to predict that large ( $\gtrsim L_*$ ) galaxies should possess massive, but diffuse (and, possibly, hard to detect) coronae of hot baryons (e.g. Fukugita & Peebles 2006; Crain et al. 2010).

Giant elliptical galaxies provide a natural laboratory for exploring these predictions. The X-ray emitting hot gas halos around many early-type galaxies (e.g. O’Sullivan et al. 2001) provide a unique opportunity to

extend to a lower mass regime the hydrostatic X-ray techniques widely employed to study the dark and baryonic matter in galaxy clusters (Buote & Humphrey 2012a, for a review). Provided the hot gas halo is sufficiently bright and morphologically relaxed, hydrostatic techniques are expected to be useful (Buote & Tsai 1995; Rasia et al. 2006; Nagai et al. 2007; Piffaretti & Valdarnini 2008; Buote & Humphrey 2012a). This is confirmed observationally by detailed comparisons between masses inferred from X-ray methods and independent stellar dynamical measurements, or the predictions of stellar population synthesis models, which suggest a typical accuracy of at least  $\sim 20\text{--}30\%$  (e.g. Churazov et al. 2008; Humphrey et al. 2008, 2009a; Shen & Gebhardt 2010; Das et al. 2010, 2011; Humphrey et al. 2012b).

Although the properties of the largest galaxies may be intertwined with that of a surrounding group or cluster (e.g. Helsdon et al. 2001; Mathews et al. 2006), there is increasing evidence that  $\sim L_*$  early-type galaxies in  $\sim$ Milky Way-mass halos can be found with hot gas detectable out at least to  $\sim R_{2500}$ . In particular, Humphrey et al. (2006) presented a hydrostatic analysis of three isolated galaxies, based on data from the *Chandra* X-ray Observatory, inferring virial masses ( $M_{\text{vir}} \lesssim 10^{13} M_{\odot}$ ). Using deep *Chandra* and *Suzaku* data, Humphrey et al. (2011) refined the analysis for one of these systems, NGC 720, confirming  $M_{\text{vir}} = (3.1 \pm 0.4) \times 10^{12} M_{\odot}$ , close to the mass of the Milky Way (Klypin et al. 2002). Other X-ray bright, fairly isolated galaxies with similar properties have been discussed by O’Sullivan & Ponman (2004),

<sup>1</sup> Department of Physics and Astronomy, University of California at Irvine, 4129 Frederick Reines Hall, Irvine, CA 92697, USA

<sup>2</sup> Harvard-Smithsonian Center for Astrophysics, 60 Garden Street, Cambridge, MA 02138, USA

<sup>3</sup> School of Physics and Astronomy, University of Birmingham, Birmingham, B15 2TT, UK

O’Sullivan et al. (2007) and Memola et al. (2011).

The extent to which typical giant elliptical galaxies possess DM halos in accord with  $\Lambda$ CDM remains unclear. Buote et al. (2007) assembled from the literature hydrostatic measurements of the virial mass and concentration ( $c_{\text{vir}} = R_{\text{vir}}/r_s$ , where  $R_{\text{vir}}$  is the virial radius and  $r_s$  is the characteristic scale of the DM halo density profile) for a sample of galaxies, groups and clusters, including the three isolated systems studied by Humphrey et al. (2006). They found, for the first time, an inverse correlation between  $c_{\text{vir}}$  and  $M_{\text{vir}}$ , with a slope close to the theoretical value, confirming a fundamental prediction of  $\Lambda$ CDM models. Still, the three isolated galaxies, constituting the low mass ( $\lesssim 10^{13}M_{\odot}$ ) end of the relation, were marginally ( $\sim 2.6\sigma$ ) more concentrated than predicted by recent theoretical models in the most favourable cosmology (the “WMAP1” model for relaxed halos reported by Macciò et al. 2008). Given the small number of objects involved, however, it is unclear whether this represents actual tension with theory, or is a consequence of selection effects or small number statistics.

To date, these represent arguably the best constraints on the DM halo concentration for individual giant elliptical galaxies that reside in galaxy-scale ( $\lesssim 10^{13}M_{\odot}$ ) halos. Lensing studies alone cannot presently resolve the mass profiles of individual galaxies, although stacked weak (and strong) lensing analysis indicates that at least some early-type galaxies can be found in  $\sim 10^{13}M_{\odot}$  DM haloes with concentrations broadly consistent with  $\Lambda$ CDM (Mandelbaum et al. 2006; Gavazzi et al. 2007). Orbit- and particle-based stellar dynamical methods are beginning to emerge that incorporate DM halos (e.g. Thomas et al. 2007; de Lorenzi et al. 2009), but there have, so far, been few published constraints on  $c_{\text{vir}}$ .

If the DM halos of early-type galaxies are well described by the NFW (Navarro et al. 1997) profile, within  $\sim$ the optical effective radius ( $R_e$ ), the baryonic component must be dominant (Buote et al. 2012). It is increasingly being recognized that the baryons and DM conspire to produce a *total* mass density profile that can be well-approximated by a powerlaw ( $\rho_{\text{tot}} \propto r^{-\alpha}$ ) over a wide radial range (e.g. Fukazawa et al. 2006; Gavazzi et al. 2007; Humphrey & Buote 2010, and references therein; Churazov et al. 2010; Duffy et al. 2010). Although typically  $\alpha \simeq 2$  is reported (Koopmans et al. 2009), Humphrey & Buote (2010) found that  $\alpha$  derived from *Chandra* observations of a sample of 10 galaxies, groups and clusters was tightly anti-correlated with  $R_e$ . This behaviour can be understood by the combination of the stellar (Sersic) and DM (NFW) profiles required to maintain an approximately powerlaw total mass distribution, and implies that the DM fraction within  $R_e$  varies systematically in such a way as to reproduce, without fine tuning, the tilt of the fundamental plane (FP). If this trend is the explanation of the tilt of the FP, it should exhibit very little intrinsic scatter, but more X-ray measurements are needed to investigate this further. The anti-correlation between  $\alpha$  and  $R_e$  has recently been confirmed by Auger et al. (2010), who used joint strong lensing and stellar kinematics measurements. While the optical results provide important verification of the X-ray work, they are limited by being confined mostly to within  $\sim R_e$ , where the DM halo is sub-dominant, and because they gener-

ally lack the resolution to resolve the mass profiles in detail. Indeed, the Auger et al. data may be slightly offset from, and exhibit more intrinsic scatter than, the X-ray relation, although more X-ray data are needed.

No census of the mass within early-type galaxies is complete without accounting for the baryons in the hot, diffuse gas. In the local Universe, the measured stellar and cold gas content of  $\sim L_*$  galaxies lies significantly below the Cosmological baryon fraction (Fukugita et al. 1998; McGaugh et al. 2010), and in tension with standard models of galaxy formation (e.g. Benson et al. 2003). Resolutions to this problem generally involve the “missing baryons” either residing in a massive, hot halo (e.g. Maller & Bullock 2004; Fukugita & Peebles 2006) or being ejected completely from the system (e.g. Dekel & Silk 1986; Oppenheimer & Davé 2006). To date most of the effort to locate these hot halos has focused on disk galaxies, where they have not yet been robustly detected (Benson et al. 2000; Anderson & Bregman 2010; Rasmussen et al. 2009). Although X-ray absorption line studies have identified hot gas around the Milky Way (e.g. Nicastro et al. 2002; Fang et al. 2002; Rasmussen et al. 2003; Fang et al. 2006; Bregman & Lloyd-Davies 2007; Buote et al. 2009; Fang et al. 2010), and there have been reports of extended X-ray emission unassociated with star formation in a disk galaxy (Anderson & Bregman 2011), whether these constitute the predicted major reservoirs of baryons depends on, generally uncertain, extrapolation (e.g. Fang et al. 2006; Rasmussen et al. 2009; Anderson & Bregman 2010, 2011).

Recently Humphrey et al. (2011) studied the hot gas around the isolated,  $\sim$ Milky Way-mass ( $M_{\text{vir}} = [3.1 \pm 0.4] \times 10^{12}$ ) elliptical galaxy NGC 720, detecting the baryons as far as  $\sim R_{2500}$ . Elliptical galaxies have a distinct advantage over disk galaxies for detecting the putative hot halos, since few of the baryons are bound up in cold gas, so the halo should be denser and more luminous than in a comparable spiral galaxy. In the case of NGC 720, the baryon fraction within  $R_{2500}$ <sup>4</sup> was tightly constrained to  $f_{b,2500} = 0.10 \pm 0.01$ , rising to  $f_b = 0.16 \pm 0.04$  by  $R_{\text{vir}}$ , consistent with the Cosmological value (0.17; Dunkley et al. 2009). Unlike the ad hoc extrapolations often employed (e.g. the isothermal  $\beta$ -model), this self-consistent evaluation of the model at large radii required only that the gas is approximately hydrostatic (as expected around an isolated system, e.g. Crain et al. 2010), and the DM mass profile is close to NFW, while being relatively insensitive to the thermodynamics of the gas outside the region where it was clearly detected. *NGC 720 therefore constitutes the most promising detection of a baryonically closed  $\sim$ Milky Way-mass halo*, which indicates that feedback need not denude such a galaxy of a large fraction of its baryons (e.g. Kauffmann et al. 2009). Whether or not NGC 720 represents an unusual case remains to be established, but may have clear implications for the location of the missing baryons in the local universe.

Although X-ray observations of galaxy-mass ( $\lesssim 10^{13}M_{\odot}$ ) halos provide a unique and powerful insight into galaxy formation, the small number of

<sup>4</sup> We define  $R_{\Delta}$  as the three dimensional radius within which the mean mass density of the system is  $\Delta$  times the critical density of the Universe.

reliable measurements of  $c_{\text{vir}}$ ,  $M_{\text{vir}}$ , baryon fraction ( $f_b$ ), and  $\alpha$  at this mass scale limits the conclusions which can be drawn. In addition to the problem of small number statistics, the current objects were chosen for study heterogeneously, potentially introducing unknown selection effects (Buote & Humphrey 2012a, for a review). To address these concerns, we initiated the Elliptical Isolated X-ray (EIIxR) Galaxy Survey, an X-ray survey of an optically selected, volume limited ( $< 110$  Mpc) sample of very isolated,  $\sim L_*$  early-type galaxies. The isolation condition eliminates most group-scale halos and ensures an accurate census of the X-ray properties in systems resembling the optical properties of NGC 720. Isolation also minimizes the likelihood that the low-density hot gas halo expected around a  $\sim$ Milky Way-mass galaxy is stripped in a dense, cluster environment. A full description of the sample, and initial results are given in Buote et al. (2012).

Not all of the EIIxR galaxies have luminous X-ray halos within  $\sim R_e$ , as might be expected given the large range of measured  $L_X$  at fixed optical luminosity in early-type galaxies (Canizares et al. 1987; O’Sullivan et al. 2001; Ellis & O’Sullivan 2006). This large scatter may indicate that both the virial mass of the halo and the feedback history of the galaxy play a role in determining  $L_X$  (Mathews et al. 2006). Since the gas emissivity depends on the square of its density, and gas density profiles are not self-similar (Humphrey et al. 2006; Gastaldello et al. 2007; Sun et al. 2009), it is difficult to map galaxies from the optical *versus* X-ray luminosity plane onto  $f_b$  directly. This means that  $L_X$ , which is typically measured within only a small fraction of the virial radius ( $R_{\text{vir}}$ ), is a poor tracer of the overall gas mass (e.g. Crain et al. 2010). While even low- $L_X$  early-type galaxies could possess massive hot coronae in which most of the gas has been pushed out to large scales, detecting them will pose similar observational challenges as for spiral galaxies (e.g. Rasmussen et al. 2009). Instead, those objects with X-ray luminous halos provide arguably the best opportunity to measure the baryons out to  $\sim$ tens of kpc, and thus provide direct constraints on the baryon fraction, at least for a subset of early-type galaxies. It is therefore of interest to define an initial X-ray luminous sub-sample of the EIIxR galaxies for further study with detailed hydrostatic methods.

In this paper, we present a detailed *Chandra* and *XMM* study of one such galaxy. NGC 1521 was identified as one of several X-ray luminous analogues to NGC 720 in a shallow, pointed *XMM* observation taken as part of the EIIxR Galaxy Survey, and was targeted for deeper follow-up. We discuss the properties of the galaxy in detail in § 2, before describing the X-ray data-reduction and analysis (§ 3), the mass modelling method (§ 4), the likely sources of systematic uncertainty (§ 5) and reaching our conclusions in § 6.

We adopted a distance of 61.2 Mpc to NGC 1521, corresponding to the redshift 0.01415 (Ogando et al. 2008), if we assume a flat cosmology with  $H_0 = 70 \text{ km s}^{-1}$  and  $\Omega_\Lambda = 0.7$ . In § 5, we show that small errors in our distance estimate will not affect our conclusions. At that distance,  $1''$  corresponds to 290 pc. We adopted  $R_{102}$  as the virial radius ( $R_{\text{vir}}$ ), based on the approximation of Bryan & Norman (1998) for the redshift of NGC 1521. Unless otherwise stated, all error-bars represent  $1-\sigma$  con-

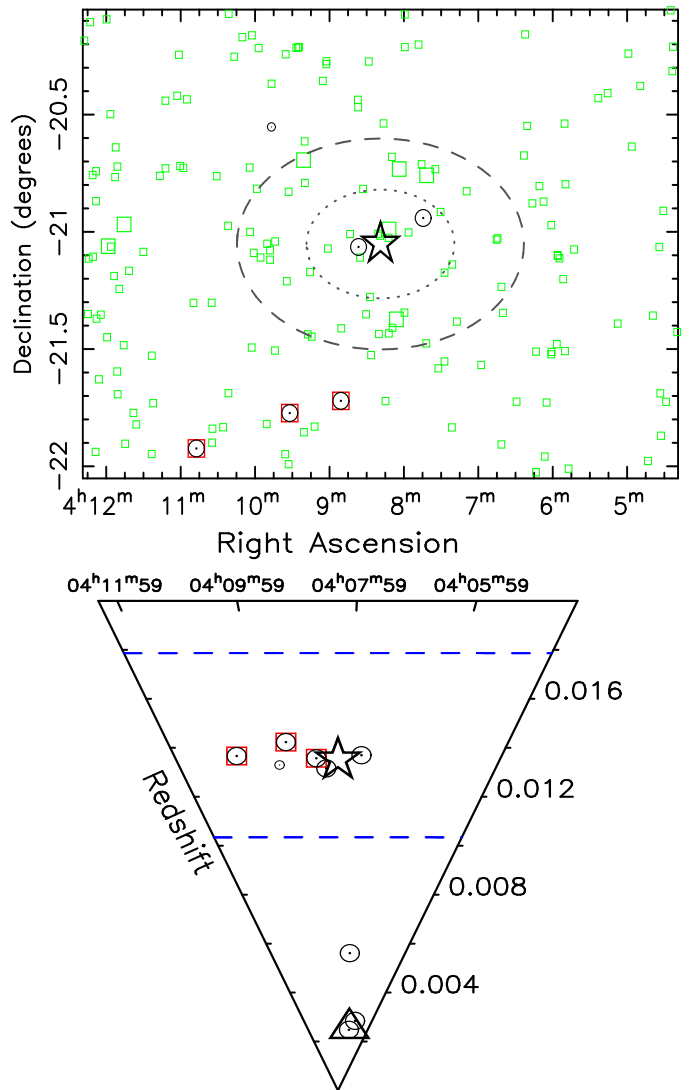


FIG. 1.— Distribution of galaxies around NGC 1521 (shown as a large star) in the *HyperLEDA* database. Galaxies with known redshift are shown as large triangles (less than 2 apparent magnitudes fainter in the B-band than NGC 1521), large circles (2–4 magnitudes fainter), or small circles (more than 4 magnitudes fainter). Galaxies with measured recessional velocities differing by more than  $1125 \text{ km s}^{-1}$  from NGC 1521 are omitted from the upper panel; none of the galaxies in the upper panel are within 2 magnitudes of NGC 1521. The corresponding redshift range is shown as dashed blue lines in the lower plot. Those galaxies in the field of view but without redshift information are shown as large squares (2–4 magnitudes fainter than NGC 1521 in the B-band or, if unavailable, in the I-band,  $K_s$  or “Opt” band, as given in *HyperLEDA*, respectively), or small squares (more than 4 magnitudes fainter). The red squares indicate the three galaxies catalogued, along with NGC 1521, as belonging to the small “group” S138 by Ramella et al. (2002). The dotted ellipse indicates the region enclosing projected  $R_{500}$ , while the dashed circle corresponds to  $R_{\text{vir}}$ . These regions appear elliptical due to the aspect ratio of the figure. NGC 1521 is clearly isolated from other bright galaxies.

fidence limits (which, for our Bayesian analysis, implies the marginalized region of parameter space within which the integrated probability is 68%).

## 2. NGC 1521

### 2.1. Target selection

The EIIxR galaxies were identified in the *HyperLEDA* database to be optically isolated,  $\sim L_*$  early-type galaxies

within 110 Mpc. For a full description of the sample selection and properties, we refer the reader to Buote et al. (2012). Briefly, we selected early-type galaxies with absolute B-band magnitude between -21.4 and -19.8, and required there to be no other galaxy within a projected distance of 750 kpc that is less than 2 apparent magnitudes fainter than the target. Where available, we used recessional velocity information to eliminate foreground or background interlopers (for which we assumed the line of sight velocities differed from the target by more than  $1125 \text{ km s}^{-1}$ ).

In Fig 1, we show the distribution of galaxies in the *HyperLEDA* database around NGC 1521. Excluding an obvious, bright foreground object (NGC 1518), none of the galaxies are less than 2 magnitudes fainter than NGC 1521, confirming its isolation from bright companions. We note that, nevertheless, the group catalogue of Ramella et al. (2002), derived using a friends-of-friends algorithm, included NGC 1521 as a member of the low-mass ( $M_{\text{vir}} \simeq 10^{13} M_{\odot}$ ) S138 “group”. The other three members of the putative group are marked in Fig 1, but all are more than 2 magnitudes fainter than NGC 1521 (so that it does not violate our isolation criterion). Furthermore, while these galaxies could be gravitationally bound to the NGC 1521 system (as the brightest member), they lie outside its virial radius (§ 4), and are not symmetrically distributed about NGC 1521, implying that S138 does not represent a virialized system (whereas NGC 1521 itself does).

## 2.2. Optical properties

In the optical, NGC 1521 exhibits complex structure. B-band isophotal analysis (Capaccioli et al. 1988) reveals an ellipticity gradient and a strong position angle twist within the central  $\sim 10$  kpc, indicating that the galaxy is not axisymmetric, and may be triaxial. Although our isolation criterion ensures that NGC 1521 is not currently undergoing a major galaxy interaction, deep B, V, R and I images taken as part of the Carnegie-Irvine Galaxy Survey (CGS; Ho et al. 2011; Li et al. 2011)<sup>5</sup> reveal faint shell-like surface brightness discontinuities outside the central  $\sim 40$  kpc, which may be the relic of a past minor merger event. Still, we note that such features may persist in the stars for several Gyr following the event (e.g. Schweizer & Seitzer 1992), while the sound crossing time of a  $\sim 40$  kpc system, assuming an ambient gas temperature  $\sim 0.5$  keV/k (similar to what is measured in NGC 1521; § 3), is only  $\sim 10^8$  yr. This means that the hot ISM will relax to an approximately hydrostatic state following a significant disturbance far faster than the stellar distribution, and so it is unsurprising that the X-ray morphology appears very relaxed (§ 3).

Accurate modelling of the mass distribution requires a reliable deprojection of the stellar light profile. To obtain this, we explored a triaxial model for the underlying stellar light distribution. Following Cappellari (2002), we approximated the stellar density profile as a series of concentric, triaxial ellipsoids with Gaussian radial profiles ( $\rho_* \propto \exp(-0.5(a_V/\sigma)^2)$ ), where  $\rho_*$  is the stellar density,  $a_V$  is the ellipsoidal coordinate  $a_V^2 = (x)^2 + (y/p)^2 + (z/q)^2$  (here  $1 \geq p \geq q$ ), and  $x$ ,

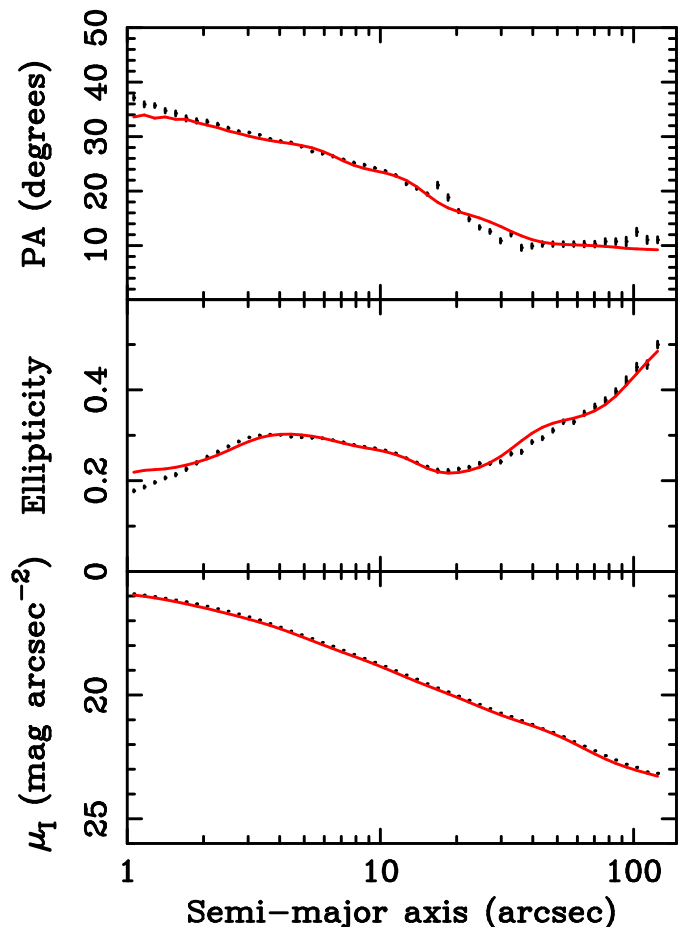


FIG. 2.— *Top panel:* I-band isophotal major-axis position angle (measured counterclockwise from the north) of NGC 1521 (data-points), derived from the Carnegie-Irvine Galaxy Survey data (Ho et al. 2011; Li et al. 2011). Overlaid is our best-fitting triaxial model (solid red line). *Center panel:* I-band ellipticity profile and best-fitting model. *Lower panel:* I-band major axis surface brightness profile of NGC 1521, shown along with our best-fitting model. The fit is good; the mean absolute residual is only 0.01 mag, which is sufficient for our purposes. Note that  $\mu_1$  differs slightly from the published profile of Li et al. (2011) since we allow the isophotal position angle and ellipticity to vary with radius during its computation.

$y$  and  $z$  are Cartesian coordinates. To simplify the deprojection, we assumed that the long, short and intermediate axes of each ellipsoid were coaligned. For any given orientation (which is completely described by three position angles,  $\theta$ ,  $\phi$  and  $\psi$ ), we projected the ellipsoid onto Cartesian sky coordinates, using Eqn 9 of Binney (1985). We used dedicated software to fit this model to the central  $4.3 \times 4.3'$  portion of the calibrated, flat-fielded I-band image produced by the CGS team (Ho et al. 2011; Li et al. 2011), while masking unrelated point sources and other galaxies. To account for seeing, we convolve the model image by a  $1.2''$  FWHM Gaussian, estimated from the broadening of stellar images near NGC 1521. We adopted the Galactic extinction correction from Schlegel et al. (1998). We allowed the position angles of the system, and the luminosity,  $\sigma$ ,  $p$  and  $q$  of each component to vary during the fit. We obtained a satisfactory fit when we employed 6 Gaussian components, and not only accurately recovered the surface brightness profile (as shown in Fig 2), but also the isophotal position angle twist to

<sup>5</sup> <http://cgs.obs.carnegiescience.edu/CGS/Home.html>

$\sim 0.5^\circ$  and the ellipticity to  $\sim 2\%$ , on average.

### 3. X-RAY DATA REDUCTION AND ANALYSIS

#### 3.1. XMM

The region of sky containing NGC 1521 was imaged by *XMM* on 4 separate occasions, as part of the ELIXR Galaxy Survey. To simplify the analysis, we consider here only the results from ObsID 0552510101, the deep, 104 ks (excluding periods of background flaring) exposure beginning on 2009 Feb 7. In our default analysis, we focus only on the EPIC MOS instruments, as we have found the calibration of the PN to be more uncertain in the low-temperature ( $kT \sim 0.5$  keV) regime, and the source is too faint for the RGS data to be useful. Still, as a systematic error check, we explore the results obtained with the PN in § 5.5. The data were reduced and analysed as described in Gastaldello et al. (2007), using the XMMSAS 10.0 software suite. Briefly, calibrated events files were generated with the `emchain` task. We filtered the list to remove known bright pixels and hot columns, and periods of high background (flaring) were identified visually in the 10–12 keV lightcurve, and excised. Data from the unexposed portions of CCD MOS1-4 exhibited an unusually high count-rate and soft spectrum, consistent with the “anomalous states” identified by Kuntz & Snowden (2008). We therefore excluded all data from this CCD in our subsequent analysis. Point sources were identified by operating on the 0.5–10 keV band images with the `ewavelet` task. The source lists from the three EPIC instruments were merged and checked visually. In subsequent analysis, we excluded data from within a  $30''$  radius aperture (corresponding to approximately 90% encircled energy) centred on each confirmed source. The image of the central MOS1 CCD is shown in Fig 3, revealing both the extended emission from NGC 1521, and a number of point sources that were excluded.

Spectra were accumulated in 8 concentric, contiguous annuli, placed at the X-ray centroid, reaching  $\sim 190$  kpc. To mitigate mixing between annuli due to the point spread function, the minimum half-width of the annuli (corresponding to the radius of the central, circular region) was set to  $30''$ , corresponding approximately to  $\sim 90\%$  encircled energy. Typical spectra are shown in Fig 4. Spectral redistribution matrix files (RMFs) and ancillary response files (ARFs) were generated with the SAS `rmfgen` and `arfgen` tasks, the latter using an exposure-corrected detector map to perform flux weighting.

The MOS1 and MOS2 spectra were fitted simultaneously in *Xspec* vers. 12.5.1n, to obtain the projected abundance, temperature and density profiles (see Humphrey et al. 2011). The data were fitted using the C-statistic, which is less subject to bias in all count rate regimes than the popular implementations of  $\chi^2$  for Poisson-distributed data (Humphrey et al. 2009b), and the fits were restricted to the 0.5–5.0 keV band (to avoid instrumental lines at higher energy). To aid convergence, we rebinned the spectra to ensure at least 20 photons per bin. We modelled the hot gas as an APEC model, and included a 7.3 keV bremsstrahlung component to account for undetected LMXBs, which was only significant within  $\sim R_e$  (4.7 kpc, from the 2MASS database: Jarrett 2000). Hot gas abundance ratios with respect to Fe were tied be-

tween all annuli. Where they could not be constrained, they were fixed at the Solar ratio (Asplund et al. 2004).

To account for the background, we adopted the approach in Humphrey et al. (2011). Specifically, to account for the instrumental and particle background, we included a broken powerlaw model (not folded through the ARF) and two Gaussians (at 1.5 keV and 1.7 keV). The normalization of the instrumental components was allowed to vary with radius, and (to improve constraints) the shape of the broken powerlaw component was tied between the inner three annuli, and between the fourth and fifth annuli. We note that Kuntz & Snowden (2008); Snowden et al. (2008) provide an alternative strategy for background subtraction (ESAS<sup>6</sup>), which we explore in detail in § 5.4. We choose not to use ESAS for our default analysis since there are inherent uncertainties in the procedure to map from the out of field of view count rates onto the instrumental background, which could cause problems in the highly background-dominated regime at the outskirts of NGC 1521. To account for the cosmic X-ray background, we included an (absorbed) powerlaw model with  $\Gamma=1.41$  (De Luca & Molendi 2004).

Given its Galactic coordinates ( $l=216^\circ$ ,  $b=-45^\circ$ ), NGC 1521 is located at the extreme edge of the larger of two adjacent excesses in the soft X-ray background, known as the “Eridanus X-ray enhancement”, that may be due to an old supernova remnant (Narayan et al. 1976; Snowden et al. 1995). Therefore, it is important to take care over the characterization of the soft X-ray background. Using pointed *XMM* observations, Henley et al. (2010) were able to characterize the Galactic background at high latitudes, including data in the vicinity of NGC 1521, with a model comprising two plasma components (one unabsorbed and one absorbed), with  $kT \sim 0.1$  keV and  $\sim 0.2$  keV, respectively (see also Kuntz & Snowden 2000). For the two pointings within  $\sim 8^\circ$  of NGC 1521 (their observations 22 and 23),  $kT$  of the hotter plasma component was constrained to  $0.197^{+0.012}_{-0.018}$  keV and  $0.189^{+0.009}_{-0.014}$  keV, respectively, which are consistent within errors. The *ROSAT* 0.1–1.0 keV count-rate in a  $0.6$ – $1.0^\circ$  region around NGC 1521<sup>7</sup> is actually within  $\sim 15\%$  of that coincident with Henley et al.’s observation 23.

Since NGC 1521 is closer to the peak of the Eridanus enhancement than these fields, the temperature of the hotter component could, plausibly, be different. To explore this, we analysed a deep ( $\sim 100$  ks) archival *Suzaku* observation of the “Eridanus Hole” (ObsID 502076010), a blank-sky region also in the outskirts of the Eridanus enhancement ( $l=213^\circ$ ,  $b=-39^\circ$ ), but where the background is  $\sim 30\%$  higher than for NGC 1521. We reduced the data as described in Humphrey et al. (2011), and extracted a spectrum from the whole field, excluding data in  $2'$  regions around bright point sources (we identified these sources by eye in the *XMM* EPIC MOS1 image of the same field (ObsID 0203900101); we used *Suzaku*, rather than *XMM* for characterizing the Galactic emission due to its lower, stabler instrumental background

<sup>6</sup> [http://heasarc.gsfc.nasa.gov/docs/xmm/xmmhp\\_xmmesas.html](http://heasarc.gsfc.nasa.gov/docs/xmm/xmmhp_xmmesas.html)

<sup>7</sup> Determined by querying the *ROSAT* diffuse X-ray background maps (Snowden et al. 1997) with the on-line HEASARC X-ray background tool, <http://heasarc.gsfc.nasa.gov/cgi-bin/Tools/xraybg/xraybg.pl>



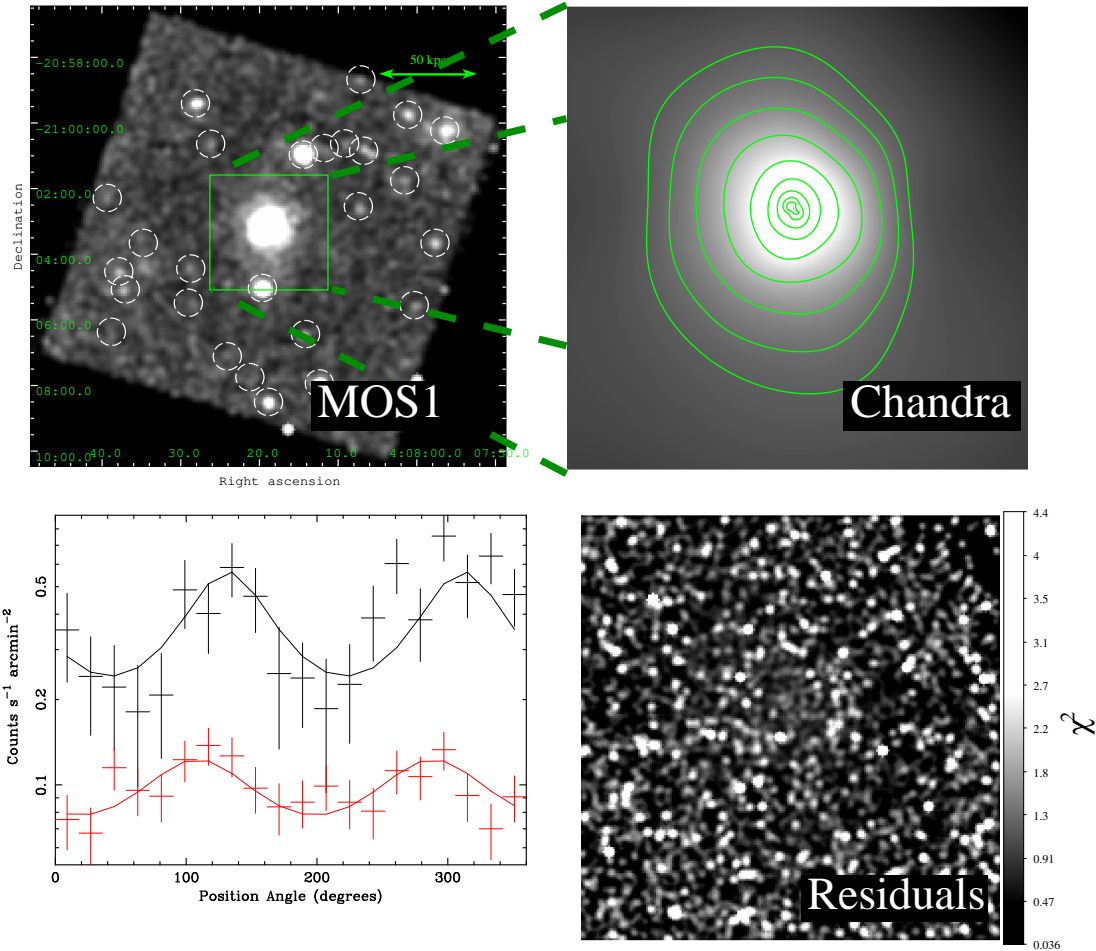


FIG. 3.— *XMM* MOS1 (central CCD; top left) and *Chandra* (top right) images of NGC 1521. Point sources found in the *XMM* image have been marked with white circles, and are excluded from subsequent analysis. Although it is not clear given the dynamic range of the *XMM* image, the emission from NGC 1521 extends to the edge of the central CCD, as we show in § 3. The *Chandra* image has been cleaned of point sources and mildly smoothed, and arbitrarily spaced isophotes overlaid to guide the eye. The smoothing scale varied from  $\sim 1''$  at the smallest scales, to  $\sim 0.9'$  (15 kpc) at the outer part of the image (see text). To explore the slight distortion of the innermost isophote, we show (bottom left), the azimuthal variation of the surface brightness in the (unsmoothed) *Chandra* image, averaged radially between 1–5'' (upper, black data-points) and between 5–15'' (lower, red data-points). The position angle is measured anticlockwise from due east. We overlay the best elliptical  $\beta$ -model fit (allowing a position angle twist between each region). We note that the slight excess between 240–300'' in the 1–5'' data is not statistically significant. At the bottom right, we show a “residual significance” image (see text) of the centre of the system, indicating deviations from a smooth fit to the *Chandra* X-ray isophotes. There is no obvious large-scale feature in this map, indicating the system is largely relaxed.

and good spectral resolution). As this is effectively a blank-sky field, after subtracting off the standard instrumental background (which was estimated by standard *Heasoft* tools; for more details, refer to Humphrey et al. 2011), the remaining spectrum represents the X-ray background. We were able to fit this in the 0.5–5.0 keV band with a model comprising a  $\Gamma = 1.41$  powerlaw, an unabsorbed 0.07 keV APEC plasma model (with Solar abundances: Asplund et al. 2004), and an absorbed APEC model with  $kT = 0.22 \pm 0.02$  keV, i.e. approximately the same model as was used by Henley et al. (2010). Although the inferred distance of the gas contributing to the Eridanus enhancement is close ( $\sim 400$  pc; e.g. Snowden et al. 1995), we found an adequate fit using the whole Galactic column for the absorbed APEC component, which may reflect the high galactic latitude of the feature. Freeing  $N_H$  did not give rise to a significantly better fit. We therefore adopted  $kT$  of 0.07 and 0.20 keV, respectively for the two APEC components in our fit, and

used the whole Galactic column density (Kalberla et al. 2005) to absorb the hotter component.

We found this background model was able to fit adequately the background spectra generated for regions corresponding to each annulus used in our *XMM* analysis from the standard “template” events files. We found that our full model was able to fit the spectra in all annuli reasonably well, as shown in Fig 4. We show the inferred Fe abundance profile and the global abundance ratios in Fig 5, and the measured temperature and density profiles in Fig 6. We note that we were able to obtain good constraints on the gas temperature and density out to 190 kpc, which is well beyond  $R_{2500}$ , and is approaching  $R_{500}$  ( $R_{2500} = 121 \pm 8$  kpc;  $R_{500} = 240 \pm 22$  kpc; § 4), which is beyond even what we achieved in our NGC 720 analysis. We expect the results not to be strongly sensitive to the treatment of the background if the ratio of the source to the background rate  $\gtrsim 0.5$  in the 0.65–0.9 keV band, corresponding to the Fe L-shell region, which is the cru-

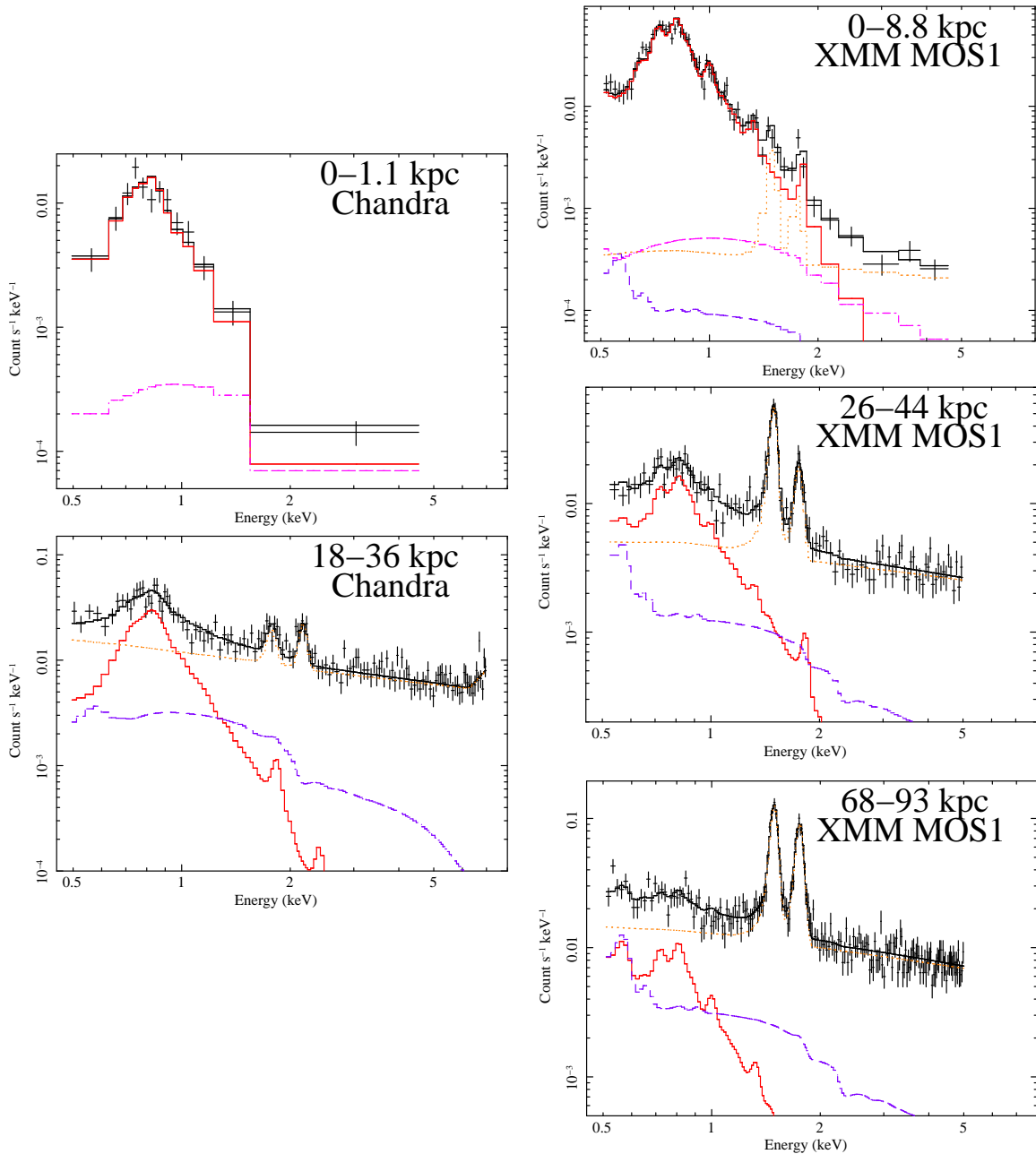


FIG. 4.— Representative *Chandra* and *XMM* MOS1 spectra for NGC 1521, shown without background subtraction. In addition to the data, we show the best-fitting model, folded through the instrumental response (solid black line), along with the decomposition of this model into its various components. We show the hot gas contribution (solid red line), the composite emission from X-ray binaries (dash-dot magenta line), the instrumental background (dotted orange) and the cosmic X-ray background (dashed purple line). The background is dominated by the instrumental component, but emission from the  $\sim 0.5$  keV gas is detectable above the background below  $\sim 1$  keV in all the spectra.

cial temperature diagnostic for a  $\sim 0.5$  keV plasma. This is true for the inner 5 *XMM* annuli, but for the outer 3 annuli, the source/ background ratio falls to  $\sim 0.22$ , 0.08 and 0.07, respectively. We explore the impact of different background subtraction subtraction methods in detail in § 5.4, finding, unsurprisingly that the outermost annuli are most sensitive to this choice, as shown in Fig 6. Nevertheless, we do not reach qualitatively different conclusions regarding the global parameters of the system (§ 5.4).

### 3.2. *Chandra*

The region of sky containing NGC 1521 was imaged by the *ACIS* instrument aboard *Chandra* (ObsID 10539; beginning on 2009 Jul 4) for a total of 49 ks good time (with periods of background flaring removed). The data were reduced and analysed as described in Humphrey et al. (2012a), using the *CIAO* 4.3 software suite and the corresponding *Chandra* calibration database (*Caldb*) vers. 4.4.2. Briefly, the data were reprocessed from the “level 1” events files, following the standard data reduction threads<sup>8</sup>. Periods of high background were identi-

<sup>8</sup> <http://cxc.harvard.edu/ciao/threads/index.html>

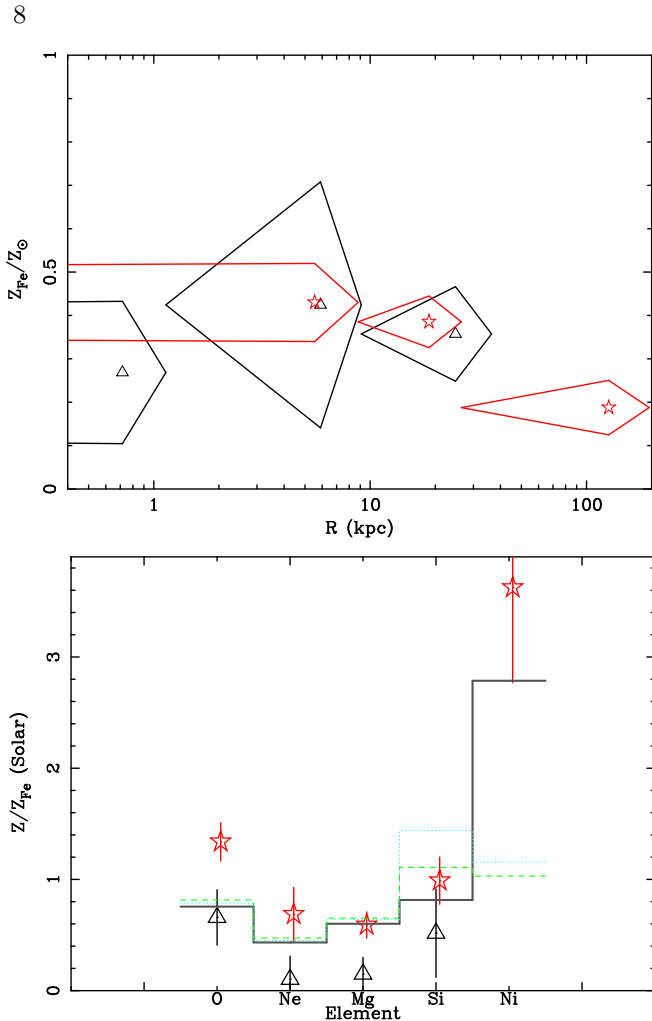


FIG. 5.— *Upper panel*: Projected Fe abundance profile, measured with *Chandra* (triangles) and *XMM* (stars). Note the overall good agreement between *Chandra* and *XMM*. *Lower panel*: Average abundance ratios with respect to Fe for the *Chandra* (triangles) and *XMM* (stars) data. The solid line is the best-fit model where the enrichment comes from SNIa and SNII, assuming the W7 SNIa yields from Nomoto et al. (1997b) and the SNII yields from Nomoto et al. (1997a). The SNIa enrichment fraction is  $0.77 \pm 0.03$ . For reference, we also show the best fits with the WDD1 (green dashed line) and WDD2 (blue dotted line) SNIa yields. All abundances are relative to the Solar abundance standard of Asplund et al. (2004).

fied by eye in the lightcurve from a low surface-brightness region of the CCDs and data from these intervals were excised. Point sources were detected in the 0.3–7.0 keV image with the *wavdetect CIAO* task. All sources were confirmed visually, and appropriate elliptical regions containing  $\sim 99\%$  of the source photons were generated. Data from these regions were excluded in subsequent analysis.

In Fig 3 (top right), we show a smoothed, flat-fielded *Chandra* image, having removed the point sources with the algorithm outlined in Fang et al. (2009). The image was smoothed with a Gaussian kernel, the width of which varied with distance from the nominal X-ray centroid according to an arbitrary powerlaw, ranging from  $\sim 1''$  at the centre of the image to  $\sim 0.9''$  at its edge. The image is smooth, albeit slightly elliptical. To search for more subtle structure we used dedicated software to fit an elliptical beta model (with constant ellipticity) to the unsmoothed (flat-fielded) image. In Fig 3 (bottom right),

we plot  $(data - model)^2 / model$ , corresponding (approximately) to the  $\chi^2$  residuals from this fit. To bring out the structure, we smoothed this image with a Gaussian kernel of width 3 pixels. The lack of significant, coherent residuals indicates that the X-ray image is very relaxed. An alternative view of the central ( $\lesssim 15''$ ) region is given in the lower left panel, which shows the azimuthal variation in the surface brightness, integrated over two radial bins. There are no statistically significant residuals from an elliptical  $\beta$ -model fit. Although the central isophotes in the smoothed *Chandra* image do appear slightly more flattened, this feature is not statistically significant, and may represent a statistical fluctuation.

Spectra and associated flux-weighted responses were extracted in a series of contiguous, concentric annuli placed at the X-ray centroid. The widths of the annuli were chosen to contain approximately the same number of background-subtracted counts, while ensuring sufficient photons for useful spectral analysis. The resulting annuli had widths larger than  $\sim 3''$ , which is sufficient to prevent spectral mixing between adjacent annuli on account of the finite spatial resolution of the mirrors. Data in the vicinity of point sources and chip gaps were excluded. The spectra were fitted simultaneously with *Xspec*, similarly to the *XMM* data, and the fit was restricted to the 0.5–7.0 keV band. To model the background, we used a similar approach to our *XMM* analysis, although the surface brightness of the background components was assumed to be constant over the region of interest (which is entirely confined to the S3 chip). Representative spectra, and the best-fitting models, resulting from a joint fit to all the *Chandra* or *XMM* data, are shown in Fig 4. The best-fitting abundance profile, and abundance ratios are given in Fig 5, while the projected temperature and density profiles are shown in Fig 6.

#### 4. MASS MODELLING

Under the hydrostatic approximation, we transformed the projected density and temperature data into mass constraints with the entropy-based “forward fitting” technique described in Humphrey et al. (2011, 2008), which enables tight control over systematic errors, in comparison with other popular methods, such as “smoothed inversion” (for a review of mass modelling methods, see Buote & Humphrey 2012a). Briefly, the entropy-based forward fitting method involves solving the equation of hydrostatic equilibrium to compute temperature and density profile models, given parametrized mass and entropy profiles. The models were then projected onto the sky and fitted to the projected temperature and density profiles, taking into account covariance between the density data points. As is standard, we assumed spherical symmetry, which does not introduce substantial biases into the inferred mass distribution (Buote & Humphrey 2012c). So as not to violate the Schwarzschild criterion for stability against convection, the entropy profile must rise monotonically, so we parametrized it as a constant plus a broken powerlaw model. We explored different models for the mass distribution, as discussed below, and allowed the parameters describing the entropy profile, plus the logarithm of the gas density at a fiducial radius, and the mass profile parameters to fit freely. Parameter space exploration



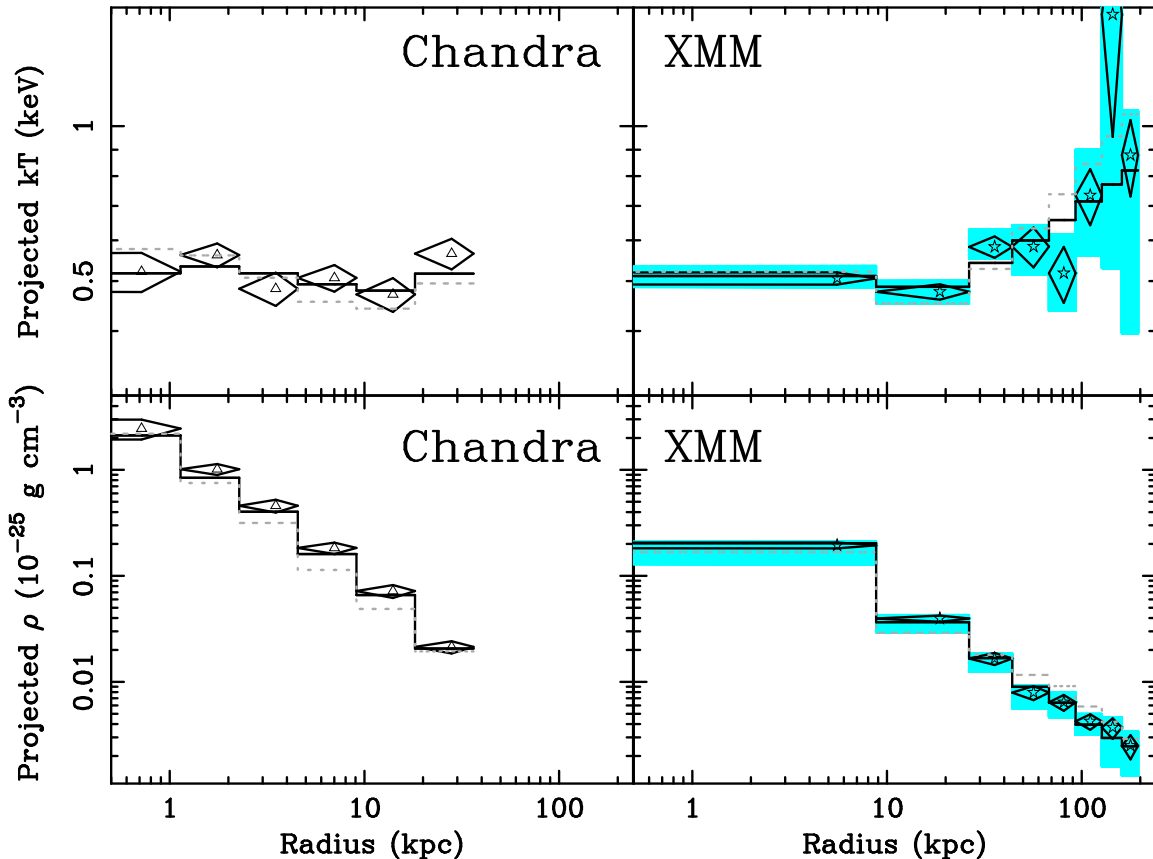


FIG. 6.— Radial temperature (top panels) and density (bottom panels) profiles for NGC 1521. We show the projected *Chandra* profiles in the left column (triangles), the projected *XMM* profiles in the right column (stars). The light blue region indicate the effect on the *XMM* density and temperature profiles of different data-analysis choices; the error-range shown combines both systematic and statistical uncertainties. Overlaid (solid lines) are the best hydrostatic model fits to each dataset, which match the data very well. The dotted lines are the best models if dark matter is omitted, for which the fit, in particular to the *XMM* data, is very poor.

employed version 2.7 of the MultiNest Bayesian code<sup>9</sup> (Feroz et al. 2009). Initially we adopted flat priors for each fit parameter, but subsequently explored the impact of this choice on the fit results (§ 5).

For the mass models, we first considered the case of no DM. We included a stellar light component, based on spherically averaging the deprojected, triaxial model for the I-band light discussed in § 2.2. As shown in Buote & Humphrey (2012c), the mass inferred from spherical hydrostatic methods should be very close to the spherically averaged true mass. The mass-to-light (M/L) ratio was allowed to fit freely. We also included a (fixed) black hole with mass  $M_{\text{BH}} = 3 \times 10^8 M_{\odot}$ , consistent with the  $M_{\text{BH}} - \sigma_*$  relation of Gültekin et al. (2009), given the central stellar velocity dispersion  $\sigma_* = 224 \text{ km s}^{-1}$  (Faber et al. 1989). The fit to the density and temperature profiles was poor ( $\chi^2/\text{dof} = 107/21$ ), as shown in Fig 6. Next, we added an NFW (Navarro et al. 1997) DM halo. We allowed  $\log_{10} M_{\text{vir}}$  and  $\log_{10} c_{\text{vir}}$  (the DM halo concentration) to fit freely (restricting  $11 \leq \log_{10} M_{\text{vir}} \leq 15$  and  $0 \leq \log_{10} c_{\text{vir}} \leq 2$ ), and obtained a formally acceptable fit ( $\chi^2/\text{dof} = 29.5/19$ ; Fig 6). The measured radial mass distribution is shown in Fig 7.

The improvement to the fit when dark matter was included was highly significant; the ratio of the Bayesian “evidence” returned for the two cases is  $1.8 \times 10^{-16}$ , im-

plying DM is required at  $8.2\text{-}\sigma$ . In Table 1, we give the stellar M/L ratio, and show the marginalized total mass within  $R_{\Delta}$  for various different overdensities ( $\Delta$ ), and the corresponding concentrations ( $c_{\Delta} = R_{\Delta}/r_s$ ;  $r_s$  is the characteristic scale of the NFW model).

In order to explore how NGC 1521 sits on the  $\alpha$ - $R_e$  relation discovered by Humphrey & Buote (2010), we experimented with fitting the data within the central 50 kpc, under the assumption that the mass density profile is given by  $\rho \propto r^{-\alpha}$ . The model fits the data comparably to the NFW+stars model discussed above, confirming that the central part of the mass profile is approximately powerlaw in form. The constraints on the mass model are summarized in Table 2. We obtained  $\alpha = 1.95^{+0.04}_{-0.06}$ , comparable to other systems in Humphrey & Buote (2010) with K-band  $R_e$  similar to NGC 1521 ( $= 4.7 \text{ kpc}$ , as given in 2MASS)<sup>10</sup>.

## 5. SYSTEMATIC ERROR BUDGET

In this section, we address the sensitivity of our results to various data analysis choices that were made. Since it is generally impractical to express these assumptions through an additional model parameter over which one can marginalize, we adopted the pragmatic approach of exploring how our results changed if the assumptions

<sup>10</sup> We used the 2MASS measurement of  $R_e$  for NGC 1521 to enable a consistent comparison with the measurements from Humphrey & Buote (2010).

<sup>9</sup> <http://www.mrao.cam.ac.uk/software/multinest/>

TABLE 1  
MASS RESULTS AND ERROR BUDGET

| Test                      | $M_*/L_I$<br>$M_\odot L_\odot^{-1}$                     | $\log M_{2500}$<br>[ $M_\odot$ ]                      | $\log c_{2500}$   | $\log M_{500}$<br>[ $M_\odot$ ]                       | $\log c_{500}$  | $\log M_{\text{vir}}$<br>[ $M_\odot$ ]                | $\log c_{\text{vir}}$                                   |
|---------------------------|---|---|---|---|---|---|---|
| Marginalized              | $2.49^{+0.26}_{-0.42}$                                  | $12.40 \pm 0.08$                                      | $0.61^{+0.16}_{-0.20}$                                  | $12.59 \pm 0.11$                                      | $0.90^{+0.15}_{-0.18}$                                  | $12.73^{+0.15}_{-0.10}$                               | $1.19^{+0.14}_{-0.17}$                                  |
| Best-fit                  | (2.55)  | (12.40)   | (0.58)  | (12.59)   | (0.88)  | (12.76)   | (1.16)  |
| $\Delta\text{DM profile}$ | $+0.34 (\pm 0.37)$                                      | $+0.02 (\pm 0.06)$                                    | ...   | $+0.16 (\pm 0.06)$                                    | ...   | $+0.36 (\pm 0.07)$                                    | ...   |
| $\Delta\text{AC}$         | $-0.652 (\pm 0.37)$                                     | $+0.008 (\pm 0.09)$                                   | $-0.086 \begin{pmatrix} +0.21 \\ -0.28 \end{pmatrix}$   | $+0.003 \begin{pmatrix} +0.15 \\ -0.11 \end{pmatrix}$ | $-0.073 \begin{pmatrix} +0.19 \\ -0.27 \end{pmatrix}$   | $+0.02 \begin{pmatrix} +0.20 \\ -0.12 \end{pmatrix}$  | $-0.072 \begin{pmatrix} +0.18 \\ -0.26 \end{pmatrix}$   |
| $\Delta\text{Stars}$      | ...   | $-0.045 (\pm 0.08)$                                   | $+0.18 \begin{pmatrix} +0.14 \\ -0.23 \end{pmatrix}$    | $-0.043 (\pm 0.11)$                                   | $+0.18 \begin{pmatrix} +0.13 \\ -0.21 \end{pmatrix}$    | $\pm 0.03 (\pm 0.13)$                                 | $+0.18 \begin{pmatrix} +0.12 \\ -0.21 \end{pmatrix}$    |
| $\Delta\text{H.E.}$       | $+0.83 \begin{pmatrix} +0.37 \\ -0.53 \end{pmatrix}$    | $+0.16 (\pm 0.09)$                                    | $+0.02 (\pm 0.20)$                                      | $+0.15 (\pm 0.12)$                                    | $+0.00 \begin{pmatrix} +0.21 \\ -0.15 \end{pmatrix}$    | $+0.17 (\pm 0.13)$                                    | $+0.00 \begin{pmatrix} +0.21 \\ -0.14 \end{pmatrix}$    |
| $\Delta\text{Background}$ | $\pm 0.13 \begin{pmatrix} +0.35 \\ -0.50 \end{pmatrix}$ | $+0.16 \begin{pmatrix} +0.12 \\ -0.07 \end{pmatrix}$  | $+0.08 \begin{pmatrix} +0.21 \\ -0.29 \end{pmatrix}$    | $+0.20 \begin{pmatrix} +0.17 \\ -0.22 \end{pmatrix}$  | $-0.07 (\pm 0.14)$                                      | $-0.11 (\pm 0.21)$                                    | $+0.23 \begin{pmatrix} +0.16 \\ -0.11 \end{pmatrix}$    |
| $\Delta\text{SWCX}$       | $-0.095 (\pm 0.42)$                                     | $-0.090 \begin{pmatrix} +0.12 \\ -0.07 \end{pmatrix}$ | $+0.11 \begin{pmatrix} +0.17 \\ -0.22 \end{pmatrix}$    | $-0.122 \begin{pmatrix} +0.16 \\ -0.09 \end{pmatrix}$ | $+0.10 \begin{pmatrix} +0.16 \\ -0.21 \end{pmatrix}$    | $-0.104 \begin{pmatrix} +0.17 \\ -0.10 \end{pmatrix}$ | $+0.10 \begin{pmatrix} +0.16 \\ -0.21 \end{pmatrix}$    |
| $\Delta\text{Instrument}$ | $+0.22 (\pm 0.31)$                                      | $+0.08 \begin{pmatrix} +0.16 \\ -0.11 \end{pmatrix}$  | $-0.243 (\pm 0.28)$                                     | $+0.15 (\pm 0.22)$                                    | $-0.219 (\pm 0.25)$                                     | $+0.18 \begin{pmatrix} +0.30 \\ -0.21 \end{pmatrix}$  | $-0.206 \begin{pmatrix} +0.21 \\ -0.26 \end{pmatrix}$   |
| $\Delta\text{Fit radius}$ | $+0.06 (\pm 0.27)$                                      | $+0.20 \begin{pmatrix} +0.10 \\ -0.13 \end{pmatrix}$  | $-0.232 (\pm 0.20)$                                     | $+0.24 (\pm 0.17)$                                    | $-0.212 (\pm 0.18)$                                     | $+0.28 (\pm 0.19)$                                    | $-0.198 (\pm 0.17)$                                     |
| $\Delta 3d$               | $-0.353 (\pm 0.53)$                                     | $-0.079 \begin{pmatrix} +0.19 \\ -0.10 \end{pmatrix}$ | $+0.03 \begin{pmatrix} +0.33 \\ -0.20 \end{pmatrix}$    | $-0.096 \begin{pmatrix} +0.24 \\ -0.13 \end{pmatrix}$ | $+0.01 \begin{pmatrix} +0.33 \\ -0.17 \end{pmatrix}$    | $-0.084 \begin{pmatrix} +0.26 \\ -0.09 \end{pmatrix}$ | $+0.03 \begin{pmatrix} +0.31 \\ -0.19 \end{pmatrix}$    |
| $\Delta\text{Fit priors}$ | $+0.39 (\pm 0.21)$                                      | $+0.06 (\pm 0.08)$                                    | $-0.296 (\pm 0.14)$                                     | $+0.15 (\pm 0.13)$                                    | $-0.275 (\pm 0.13)$                                     | $+0.19 (\pm 0.14)$                                    | $-0.261 (\pm 0.13)$                                     |
| $\Delta\text{Spectral}$   | $-0.194 \begin{pmatrix} +0.24 \\ -0.33 \end{pmatrix}$   | $-0.043 (\pm 0.06)$                                   | $+0.04 (\pm 0.15)$                                      | $-0.051 (\pm 0.09)$                                   | $+0.03 (\pm 0.14)$                                      | $-0.027 (\pm 0.10)$                                   | $+0.03 (\pm 0.13)$                                      |
| $\Delta\text{Entropy}$    | $+0.03 \begin{pmatrix} +0.23 \\ -0.45 \end{pmatrix}$    | $-0.006 \begin{pmatrix} +0.10 \\ -0.07 \end{pmatrix}$ | $-0.010 (\pm 0.19)$                                     | $-0.018 \begin{pmatrix} +0.15 \\ -0.09 \end{pmatrix}$ | $-0.010 (\pm 0.17)$                                     | $+0.01 \begin{pmatrix} +0.16 \\ -0.12 \end{pmatrix}$  | $-0.028 (\pm 0.17)$                                     |
| $\Delta\text{Weighting}$  | $-0.158 (\pm 0.44)$                                     | $\pm 0 (\pm 0.09)$                                    | $+0.04 \begin{pmatrix} +0.19 \\ -0.23 \end{pmatrix}$    | $-0.025 \begin{pmatrix} +0.16 \\ -0.10 \end{pmatrix}$ | $+0.005 (\pm 0.19)$                                     | $-0.015 \begin{pmatrix} +0.19 \\ -0.11 \end{pmatrix}$ | $+0.03 (\pm 0.19)$                                      |
| $\Delta\text{Distance}$   | $+0.59 \begin{pmatrix} +0.36 \\ -0.49 \end{pmatrix}$    | $-0.054 \begin{pmatrix} +0.11 \\ -0.07 \end{pmatrix}$ | $\pm 0.08 \begin{pmatrix} +0.20 \\ -0.24 \end{pmatrix}$ | $-0.080 \begin{pmatrix} +0.16 \\ -0.08 \end{pmatrix}$ | $\pm 0.08 \begin{pmatrix} +0.18 \\ -0.22 \end{pmatrix}$ | $+0.00 \begin{pmatrix} +0.19 \\ -0.11 \end{pmatrix}$  | $\pm 0.08 \begin{pmatrix} +0.17 \\ -0.21 \end{pmatrix}$ |
| $\Delta\text{Covariance}$ | $+0.16 \begin{pmatrix} +0.35 \\ -0.82 \end{pmatrix}$    | $+0.05 \begin{pmatrix} +0.13 \\ -0.09 \end{pmatrix}$  | $+0.07 \begin{pmatrix} +0.23 \\ -0.32 \end{pmatrix}$    | $+0.09 \begin{pmatrix} +0.20 \\ -0.12 \end{pmatrix}$  | $+0.07 \begin{pmatrix} +0.22 \\ -0.31 \end{pmatrix}$    | $+0.13 \begin{pmatrix} +0.24 \\ -0.12 \end{pmatrix}$  | $+0.06 \begin{pmatrix} +0.21 \\ -0.30 \end{pmatrix}$    |

NOTE. — Marginalized values and  $1\text{-}\sigma$  confidence regions for the stellar mass-to-light ( $M_*/L_K$ ) ratio and the enclosed mass and concentration measured at various overdensities. Since the best-fitting parameters need not be identical to the marginalized values, we also list the best-fitting values for each parameter (in parentheses). In addition to the statistical errors, we also show estimates of the error budget from possible sources of systematic uncertainty. We consider a range of different systematic effects, which are described in detail in § 5; specifically we evaluate the effect of the choice of dark matter halo model ( $\Delta\text{DM}$ ), adiabatic contraction ( $\Delta\text{AC}$ ), treatment of the stellar light ( $\Delta\text{Stars}$ ), plausible deviations from hydrostatic equilibrium ( $\Delta\text{H.E.}$ ), treatment of the background ( $\Delta\text{Background}$ ) and the Solar wind charge exchange X-ray component ( $\Delta\text{SWCX}$ ), the instrumental inter-calibration ( $\Delta\text{Instrument}$ ), the radial coverage of the data being fitted ( $\Delta\text{Fit radius}$ ), deprojection ( $\Delta 3d$ ), priors on the model parameters ( $\Delta\text{Fit priors}$ ), spectral fitting choices ( $\Delta\text{Spectral}$ ), the parameterization of the entropy model ( $\Delta\text{Entropy}$ ), removing the emissivity correction ( $\Delta\text{Weighting}$ ), distance uncertainties ( $\Delta\text{Distance}$ ), and the treatment of covariance between the temperature and density data-points ( $\Delta\text{Covariance}$ ). We list the change in the marginalized value of each parameter for every test and, in parentheses, the statistical uncertainty on the parameter determined from the test. Note that the systematic error estimates should *not* in general be added in quadrature with the statistical error. Since there is no theoretical interest in the distribution of scale radii for the cored logarithmic DM model, we do not include changes on the concentration in our error budget for this choice of profile ( $\Delta\text{DM profile}$ ). Likewise, the tests involving different stellar light modelling approaches ( $\Delta\text{Stars}$ ) involved using light profiles from different optical filter, and so we omit the  $M_*/L_I$  ratio from the error budget for that choice.

were adjusted in an arbitrary, but representative, way. We focused on those systematic effects likely to have the greatest impact on our conclusions. In Tables 1–3, we list the change in the marginalized value of each parameter. We discuss each test in more detail below. In summary, most of the inferred systematic errors are comparable to the statistical errors. For a couple of the tests, marginally significant ( $\sim 2\text{-}\sigma$ ) increases in  $M_{\text{vir}}$ , and corresponding reductions in  $f_{b,\text{vir}}$  are seen (by as much as  $\sim 0.07$ ), but our conclusions are not strongly affected.

### 5.1. Dark matter halo

The accurate computation of the gas distribution out to  $R_{\text{vir}}$  is contingent upon the accurate modelling of the gravitating mass distribution. While the NFW DM halo model is well-motivated theoretically, we also considered the “cored logarithmic” model that is sometimes used in stellar dynamical studies (e.g. Binney & Tremaine 2008; Shen & Gebhardt 2010). This model requires a slightly higher  $M_{\text{vir}}$ , and correspondingly lower  $f_{b,\text{vir}}$  (“ $\Delta\text{DM profile}$ ” in Tables 1 and 3). Although we cannot distinguish between the NFW and cored logarithmic model on the basis of  $\chi^2$  alone, the ratio of the Bayesian evidence ( $7 \times 10^{-4}$ ) implies that the cored logarithmic model, with

the adopted priors (a flat prior on the asymptotic circular velocity, between 10 and 2000  $\text{km s}^{-1}$ , and a flat prior on  $\log_{10} r_c$ , where  $r_c$  is the core radius, over the range  $0 \leq \log_{10} r_c \leq 3$ .) is a poorer description of the data at  $\sim 3.4\text{-}\sigma$ .

A theoretical modification to the DM profile is expected to arise from adiabatic contraction (Blumenthal et al. 1986; Gnedin et al. 2007; Abadi et al. 2010), which causes the halo to become cuspier due to the gravitational influence of the baryons. Modifying the NFW profile with the algorithm of Gnedin et al. (2004)<sup>11</sup>, has only a very slight effect on the best-fitting mass model (“ $\Delta\text{AC}$ ” in Tables 1 and 3), except for the stellar  $M/L$  ratio, which is reduced to make room for the increased DM fraction predicted in the inner parts of the galaxy.

### 5.2. Stellar light

Accurately decomposing the gravitating mass distribution into the luminous and dark components requires an accurate model for the (deprojected) stellar light. In the case of NGC 1521, we used a triaxial deprojection

<sup>11</sup> Using the CONTRA code publicly available from <http://www.astro.lsa.umich.edu/~ognedin/contra/>

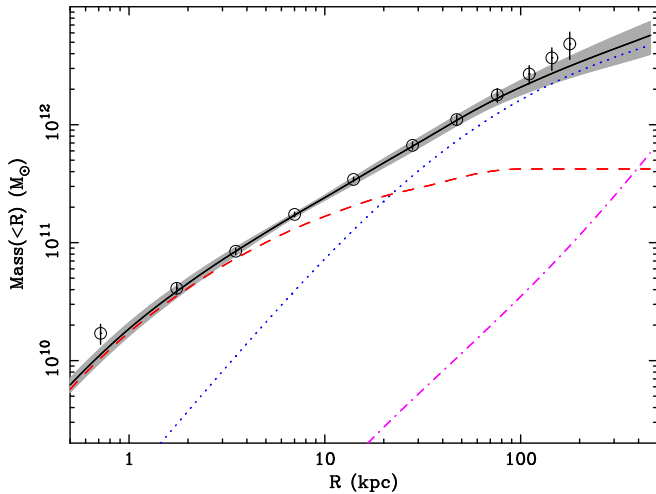


FIG. 7.— Radial mass profile of NGC 1521. The solid (black) line indicates the total enclosed mass (and the grey shaded region indicates the  $1\text{-}\sigma$  error in the total mass distribution), the dashed (red) line indicates the stellar mass, the dotted (blue) line is the dark matter, and the dash-dot (magenta) line is the gas mass contribution. Overlaid are a set of data-points derived from a more traditional “smoothed inversion” approach (Buote & Humphrey 2012a; Humphrey et al. 2009a). We stress that the model is *not* fitted to these data, but is derived independently from the temperature and density data.

TABLE 2  
MASS SLOPE RESULTS AND ERROR BUDGET

| Test                | $\log M_{75}$<br>[ $M_{\odot}$ ]              | $\alpha$  |
|---------------------|---|---|
| $\Delta$ H.E.       | +0.03 ( $\pm 0.05$ )                          | +0.04 ( $\pm 0.05$ )                              |
| $\Delta$ Background | +0.02 ( $\pm 0.06$ )<br>-0.03 ( $\pm 0.06$ )  | +0.05 ( $\pm 0.05$ )<br>-0.02 ( $\pm 0.05$ )      |
| $\Delta$ SWCX       | +0.01 ( $\pm 0.06$ )<br>-0.05 ( $\pm 0.06$ )  | -0.10 ( $\pm 0.05$ )                              |
| $\Delta$ Instrument | +0.12 ( $\pm 0.06$ )<br>-0.03 ( $\pm 0.06$ )  | +0.03 ( $\pm 0.06$ )<br>-0.10 ( $\pm 0.06$ )      |
| $\Delta$ Fit radius | +0.03 ( $\pm 0.04$ )<br>-0.03 ( $\pm 0.04$ )  | -0.028 ( $\pm 0.03$ )<br>-0.05 ( $\pm 0.03$ )     |
| $\Delta$ 3d         | +0.05 ( $\pm 0.07$ )                          | -0.075 ( $\pm 0.06$ )                             |
| $\Delta$ Fit priors | +0.01 ( $\pm 0.06$ )<br>-0.00 ( $\pm 0.06$ )  | +0.01 ( $\pm 0.06$ )<br>-0.01 ( $\pm 0.06$ )      |
| $\Delta$ Spectral   | -0.020 ( $\pm 0.04$ )                         | +0.008 ( $\pm 0.04$ )                             |
| $\Delta$ Entropy    | -0.023 ( $\pm 0.05$ )                         | +0.02 ( $\pm 0.05$ )                              |
| $\Delta$ Weighting  | +0.03 ( $\pm 0.05$ )<br>-0.06 ( $\pm 0.05$ )  | -0.033 ( $\pm 0.07$ )<br>-0.04 ( $\pm 0.07$ )     |
| $\Delta$ Distance   | -0.037 ( $\pm 0.05$ )<br>-0.06 ( $\pm 0.05$ ) | +0.03 ( $\pm 0.05$ )                              |
| $\Delta$ Covariance | +0.05 ( $\pm 0.07$ )<br>-0.03 ( $\pm 0.07$ )  | $\pm 0.04$ ( $\pm 0.06$ )<br>-0.10 ( $\pm 0.06$ ) |

NOTE. — Marginalized values and  $1\text{-}\sigma$  confidence regions for the enclosed mass at 75 kpc ( $M_{75}$ ) and the negative logarithmic slope of the mass profile ( $\alpha$ ), when fitting only a single powerlaw to the total mass distribution. We also provide the best-fitting parameters in parentheses, and a breakdown of possible sources of systematic uncertainty, following Table 1.

procedure (§ 2.2). Although we averaged this profile spherically for use with our X-ray modelling code, we have previously shown that this approach does not generally introduce significant biases (Buote & Humphrey 2012b,c). Nevertheless, the deprojection procedure may not be unique, and so it is important to explore how sensitive our results are to the details of the stellar light modelling.

We experimented with three alternative prescriptions for deprojecting the stellar light. First, we fitted the

B-band surface brightness profiles along the major and minor axis published by Capaccioli et al. (1988) with a model comprising 6 multiple, concentric 3-dimensional Gaussian density distributions, that were projected onto the sky, assuming an edge-on, oblate geometry. This ignores the isophotal twist. Second, we fitted the K-band 2MASS image in the central  $\sim 4'$  region with a model comprising an elliptical Sersic model, which we deprojected with the formula of Prugniel & Simien (1997), assuming an edge-on oblate spheroidal geometry. Finally, we adopted a spherical, deprojected de Vaucouleurs model, the effective radius and luminosity of which were set to match the catalogued 2MASS K-band values. We found that the treatment of the stellar light primarily only affected the total stellar mass, so that  $f_{b,2500}$  is very sensitive to this choice. However, by  $R_{\text{vir}}$  the impact is much less significant (“ $\Delta$ Stars” in Tables 1 and 3).

### 5.3. Hydrostatic equilibrium

Although the gas in morphologically relaxed early-type galaxies is expected to be close to hydrostatic, recent work suggests that a small amount ( $\lesssim 30\%$ ) of nonthermal support is present in the very central parts of some galaxies (e.g. Churazov et al. 2008; Das et al. 2010; Humphrey et al. 2012b). To investigate whether deviations from hydrostatic equilibrium at this level would quantitatively affect our conclusions, we modified the hydrostatic equation used in our modelling code to include a plausible nonthermal component. First we considered a nonthermal pressure fraction profile similar to that inferred for the galaxy NGC 4649, which was fixed at  $\sim 25\%$  at the centre and fell to  $\sim 10\%$  by 20 kpc, vanishing outside 30 kpc (Humphrey et al. 2012b). This is similar to the implied nonthermal pressure profiles that have been inferred in (albeit a handful of) other systems (e.g. Das et al. 2010). Since the nonthermal pressure is most important in the central few kpc, we found that adding this component did not significantly affect the global parameters of the system, although the stellar M/L ratio was increased by  $\sim 18\%$  to compensate. As a more extreme alternative, we also considered a uniform nonthermal pressure fraction fixed at 25%, similar in magnitude to that inferred from previous studies of the central parts of galaxies (e.g. Churazov et al. 2008, 2010; Humphrey et al. 2009a, 2012b; Das et al. 2010). In this case, the stellar M/L ratio was increased more substantially (by  $\sim 33\%$ ), and the global mass raised by  $\sim 0.15$  dex. Conversely, the baryon and gas fractions at fixed overdensity were found to be relatively insensitive to this choice, since *both* stellar and gas mass are increased, while the slightly larger  $R_{500}$ , for example, encloses more gas (“ $\Delta$ H.E.” in Tables 1–3).

### 5.4. Background

Since the data were background-dominated in the outer *XMM* annuli, the treatment of the background was a potentially serious source of systematic uncertainty. To investigate the extent to which our results are sensitive to this, we explored a number of different choices in our background treatment. First, for the *Chandra* data, we adopted the standard blank-field events files distributed with the CALDB to extract a background spectrum for each annulus. Since the blank-field files for each CCD

TABLE 3  
BARYON FRACTION RESULTS AND ERROR BUDGET

| Test                | $f_{g,2500}$  | $f_{g,500}$  | $f_{g,vir}$  | $f_{b,2500}$   | $f_{b,500}$  | $f_{b,vir}$  |
|---------------------|---|--|--|--|--|--|
| Marginalized        | $0.019 \pm 0.002$   | $0.040^{+0.006}_{-0.008}$  | $0.10 \pm 0.02$  | $0.16 \pm 0.03$  | $0.13 \pm 0.03$  | $0.16 \pm 0.03$  |
| Best-fit            | (0.018)   | (0.039)  | (0.095)  | (0.178)  | (0.142)  | (0.165)  |
| $\Delta$ DM profile | $\pm 0 (\pm 0.002)$   | $-0.007 (\pm 0.005)$   | $-0.029 (\pm 0.01)$  | $+0.005 (\pm 0.04)$  | $-0.021 (\pm 0.02)$  | $-0.056 \left( \begin{smallmatrix} +0.02 \\ -0.02 \end{smallmatrix} \right)$   |
| $\Delta$ AC         | $\pm 0 (\pm 0.002)$   | $-0.001 \left( \begin{smallmatrix} +0.01 \\ -0.01 \end{smallmatrix} \right)$   | $-0.007 (\pm 0.02)$  | $-0.042 (\pm 0.02)$  | $-0.026 \left( \begin{smallmatrix} +0.02 \\ -0.02 \end{smallmatrix} \right)$ | $-0.023 (\pm 0.03)$  |
| $\Delta$ Stars      | $\pm 0 (\pm 0.003)$   | $\pm 0 (\pm 0.01)$   | $+0.009 (\pm 0.02)$  | $-0.085 \left( \begin{smallmatrix} +0.03 \\ -0.02 \end{smallmatrix} \right)$ | $-0.049 (\pm 0.02)$  | $-0.029 (\pm 0.03)$  |
| $\Delta$ H.E.       | $-0.003 (\pm 0.002)$  | $-0.007 (\pm 0.01)$  | $-0.015 (\pm 0.02)$  | $\pm 0.02 (\pm 0.03)$  | $\begin{smallmatrix} +0.01 \\ -0.01 \end{smallmatrix} (\pm 0.03)$            | $\begin{smallmatrix} +0.01 \\ -0.02 \end{smallmatrix} (\pm 0.04)$  |
| $\Delta$ Background | $-0.007 (\pm 0.003)$  | $\begin{smallmatrix} +0.002 \\ -0.018 \end{smallmatrix} (\pm 0.01)$  | $\begin{smallmatrix} +0.01 \\ -0.05 \end{smallmatrix} (\pm 0.03)$  | $\begin{smallmatrix} +0.01 \\ -0.04 \end{smallmatrix} (\pm 0.04)$            | $\begin{smallmatrix} +0.02 \\ -0.04 \end{smallmatrix} (\pm 0.03)$            | $\begin{smallmatrix} +0.02 \\ -0.06 \end{smallmatrix} (\pm 0.05)$  |
| $\Delta$ SWCX       | $+0.001 (\pm 0.003)$  | $+0.004 (\pm 0.01)$  | $+0.007 (\pm 0.03)$  | $+0.006 \left( \begin{smallmatrix} +0.04 \\ -0.04 \end{smallmatrix} \right)$ | $+0.009 \left( \begin{smallmatrix} +0.04 \\ -0.03 \end{smallmatrix} \right)$ | $+0.02 (\pm 0.05)$   |
| $\Delta$ Instrument | $\pm 0 \left( \begin{smallmatrix} +0.002 \\ -0.004 \end{smallmatrix} \right)$     | $-0.006 \left( \begin{smallmatrix} +0.01 \\ -0.01 \end{smallmatrix} \right)$   | $-0.023 \left( \begin{smallmatrix} +0.03 \\ -0.03 \end{smallmatrix} \right)$   | $-0.029 (\pm 0.03)$  | $-0.025 \left( \begin{smallmatrix} +0.03 \\ -0.04 \end{smallmatrix} \right)$ | $-0.046 (\pm 0.05)$  |
| $\Delta$ Fit radius | $-0.004 \left( \begin{smallmatrix} +0.003 \\ -0.003 \end{smallmatrix} \right)$    | $-0.011 \left( \begin{smallmatrix} +0.01 \\ -0.01 \end{smallmatrix} \right)$   | $-0.059 \left( \begin{smallmatrix} +0.04 \\ -0.02 \end{smallmatrix} \right)$   | $-0.056 \left( \begin{smallmatrix} +0.03 \\ -0.02 \end{smallmatrix} \right)$ | $-0.049 (\pm 0.03)$  | $-0.071 (\pm 0.04)$  |
| $\Delta$ 3d         | $+0.004 (\pm 0.006)$  | $+0.02 \left( \begin{smallmatrix} +0.02 \\ -0.03 \end{smallmatrix} \right)$  | $+0.05 \left( \begin{smallmatrix} +0.06 \\ -0.11 \end{smallmatrix} \right)$  | $-0.036 \left( \begin{smallmatrix} +0.05 \\ -0.03 \end{smallmatrix} \right)$ | $+0.002 (\pm 0.05)$  | $+0.04 \left( \begin{smallmatrix} +0.08 \\ -0.12 \end{smallmatrix} \right)$  |
| $\Delta$ Fit priors | $\pm 0 (\pm 0.003)$   | $-0.005 (\pm 0.01)$  | $-0.019 (\pm 0.02)$  | $\begin{smallmatrix} +0.00 \\ -0.01 \end{smallmatrix} (\pm 0.03)$            | $\begin{smallmatrix} +0.00 \\ -0.01 \end{smallmatrix} (\pm 0.03)$            | $-0.030 (\pm 0.04)$  |
| $\Delta$ Spectral   | $+0.002 (\pm 0.002)$  | $+0.004 \left( \begin{smallmatrix} +0.005 \\ -0.008 \end{smallmatrix} \right)$   | $+0.01 \left( \begin{smallmatrix} +0.02 \\ -0.02 \end{smallmatrix} \right)$  | $\pm 0 (\pm 0.02)$   | $+0.01 \left( \begin{smallmatrix} +0.02 \\ -0.02 \end{smallmatrix} \right)$  | $+0.02 \left( \begin{smallmatrix} +0.03 \\ -0.03 \end{smallmatrix} \right)$  |
| $\Delta$ Entropy    | $\pm 0 \left( \begin{smallmatrix} +0.003 \\ -0.002 \end{smallmatrix} \right)$     | $\pm 0 (\pm 0.01)$   | $-0.003 \left( \begin{smallmatrix} +0.02 \\ -0.03 \end{smallmatrix} \right)$   | $-0.013 \left( \begin{smallmatrix} +0.03 \\ -0.02 \end{smallmatrix} \right)$ | $-0.005 (\pm 0.03)$  | $-0.009 (\pm 0.03)$  |
| $\Delta$ Weighting  | $-0.003 \left( \begin{smallmatrix} +0.003 \\ -0.002 \end{smallmatrix} \right)$    | $-0.006 (\pm 0.01)$  | $-0.012 \left( \begin{smallmatrix} +0.02 \\ -0.02 \end{smallmatrix} \right)$   | $-0.019 (\pm 0.03)$  | $-0.012 (\pm 0.03)$  | $-0.015 \left( \begin{smallmatrix} +0.03 \\ -0.04 \end{smallmatrix} \right)$   |
| $\Delta$ Distance   | $\pm 0.003 \left( \begin{smallmatrix} +0.003 \\ -0.002 \end{smallmatrix} \right)$ | $\begin{smallmatrix} +0.004 \\ -0.006 \end{smallmatrix} \left( \begin{smallmatrix} +0.01 \\ -0.01 \end{smallmatrix} \right)$ | $\pm 0.01 (\pm 0.02)$  | $\pm 0.03 (\pm 0.03)$  | $\begin{smallmatrix} +0.02 \\ -0.02 \end{smallmatrix} (\pm 0.03)$            | $\begin{smallmatrix} +0.03 \\ -0.01 \end{smallmatrix} \left( \begin{smallmatrix} +0.04 \\ -0.04 \end{smallmatrix} \right)$ |
| $\Delta$ Covariance | $\pm 0 (\pm 0.002)$   | $\begin{smallmatrix} +0.002 \\ -0.004 \end{smallmatrix} \left( \begin{smallmatrix} +0.01 \\ -0.01 \end{smallmatrix} \right)$ | $\begin{smallmatrix} +0.005 \\ -0.012 \end{smallmatrix} \left( \begin{smallmatrix} +0.03 \\ -0.03 \end{smallmatrix} \right)$ | $-0.017 (\pm 0.03)$  | $-0.010 (\pm 0.03)$  | $-0.015 (\pm 0.04)$  |

NOTE. — Marginalized values and 1- $\sigma$  confidence regions for the gas fraction ( $f_{g,\Delta}$ ) and baryon fraction ( $f_{b,\Delta}$ ) measured at various overdensities ( $\Delta$ ). We also provide the best-fitting parameters in parentheses, and a breakdown of possible sources of systematic uncertainty, following Table 1.

have different exposures, spectra were accumulated for each CCD individually, scaled to a common exposure time and then added. The spectra were renormalized to match the observed count-rate in the 9–12 keV band. These “template” spectra were then used as a background in *Xspec*, and the background model components were omitted from our fit. This did not strongly affect our conclusions.

Since the non X-ray component dominates the *XMM* background for much of the band-pass, we explored an alternative means of accounting for it. Specifically, we adopted the ESAS algorithm (Kuntz & Snowden 2008; Snowden et al. 2008). This involves choosing non X-ray background template files that match the count-rate and hardness ratios of photons in the unexposed portions of the CCDs. We added the X-ray background and instrumental lines, as in our standard modelling procedure. Using this approach, we found a modest reduction in the gas density at all radii (Fig 6). In the innermost regions this arises due to a slightly higher best-fitting abundance ( $Z_{\text{Fe}} \simeq 0.6$ ). Although this lowers the baryon fraction slightly (by 4% at  $R_{500}$ ), this change is comparable to the statistical error. Next, we explored the impact of varying the X-ray background. We varied the slope of the cosmic X-ray component (powerlaw model) by  $\pm 5\%$ , changed kT of the local hot bubble component to 0.1 keV, and varied kT for the galactic hot gas component between 0.18 keV and 0.24 keV, which span the range of temperatures obtained from fitting nearby blank-sky fields (§ 3.1). Although these choices had a measurable impact on the global parameters we derived for NGC 1521, our conclusions were largely unaffected. We summarize the

results in Tables 1–3 (“ $\Delta$ Background”).

#### 5.4.1. Solar Wind Charge Exchange

A potentially relevant, time variable, soft background component can arise due to the interaction of the Solar wind with interstellar material and the Earth’s exosphere. To explore the possible importance of this “Solar Wind Charge Exchange” (SWCX) component, we used data from the WIND-SWE experiment (Ogilvie et al. 1995)<sup>12</sup> to identify periods of strong Solar wind activity. Following Snowden et al. (2004), we assumed the SWCX component is negligible for a Solar wind proton flux level measured to be  $\lesssim 3 \times 10^8 \text{ cm}^{-2} \text{ s}^{-1}$ , and excised all other data. While this eliminated  $\sim 30\%$  of both the *Chandra* and *XMM* exposures, we found that this choice only had a minimal impact on the derived parameters (“ $\Delta$ SWCX” in Tables 1–3), indicating that the SWCX is not a significant problem in our analysis.

#### 5.5. Instrumental inter-calibration

In our default *XMM* analysis, we considered only the MOS1 and MOS2 instruments, as we have found the calibration of the PN to be more uncertain in the low-temperature (kT $\sim$ 0.5 keV) regime. Nevertheless, given its large collecting area, it is important to investigate whether the PN data can add information in the low surface brightness outer regions of the galaxy. To explore this, we first fitted the PN spectra, similarly to the MOS data, to obtain the gas temperature and density profile out to  $\sim 200$  kpc. We then fitted these profiles in tandem with the *Chandra* data. Although the derived  $M_{\text{vir}}$

<sup>12</sup> [http://web.mit.edu/space/www/wind\\_data.html#Protons](http://web.mit.edu/space/www/wind_data.html#Protons)

was slightly larger (and, consequently,  $f_{\text{gas}}$  and  $f_{\text{b}}$  values were smaller) than our best fitting case, the results were mostly consistent within errors (“ $\Delta$ Instrument” in Tables 1–3).

### 5.6. Radial coverage

The constraints on the global galaxy properties, especially those derived from a full mass decomposition, can be sensitive to the radial range being fitted (e.g. Gastaldello et al. 2007). To explore the sensitivity of our results to this choice, we restricted the radial range in our fit to  $\lesssim 100$  kpc (by excluding the outer three *XMM* datapoints). This increased the mass of the system by 0.28 dex (simultaneously reducing  $f_{\text{gas}}$  and  $f_{\text{b}}$ ), but only at the expense of larger error bars (“ $\Delta$ Fit radius” in Tables 1 and 3).

For the powerlaw fits to the total mass distribution, by default we excluded all data outside  $\sim 50$  kpc. Since the mass profile must deviate from a pure powerlaw at large scales, we explored the impact on our results of extending to slightly larger scales in the fit (out to  $\sim 70$  kpc). This did not affect our results significantly (“ $\Delta$ Fit radius” in Table 2).

### 5.7. Projection/ Deprojection

In this work, we fitted the projected, rather than the deprojected data. To determine the mass profile, we modelled the projected temperature and density in each annulus by evaluating the hydrostatic model for the temperature and density in three dimensions, and projecting it onto the line of sight. In general, this procedure leads to smaller statistical error bars, but may introduce additional systematic uncertainties related to how the projected quantities are computed (e.g. Gastaldello et al. 2007). To explore the likely impact of these effects, we performed a spherical deprojection by adding multiple “vapec” plasma models in each annulus, with the relative normalizations tied appropriately (e.g. Kriss et al. 1983). While functionally identical to the “project” model in *Xspec*, this allowed data from both MOS detectors to be fitted simultaneously. Given the amplification of noise by the deprojection procedure (e.g. § 3.3 of Buote 2000a; Finoguenov & Ponman 1999), we excluded the (noisy) outer three *XMM* annuli from this analysis. To account for emission projected into the line of sight from regions outside the outermost annuli, we added an APEC plasma component to the spectral model with an abundance 0.2 (consistent with the outermost annuli) and the temperature and normalization determined in each annulus from projecting onto the line of sight the best-fitting gas temperature and density models evaluated beyond the outer bin.

Although we found no evidence of biases when comparing the projected and deprojected results, the reduction in radial range fitted, in conjunction with the amplification of error bars during deprojection, resulted in much poorer constraints on the global quantities computed within  $R_{\text{vir}}$ . Nevertheless, at smaller scales (e.g.  $R_{2500}$ ), the results were much more robust (“ $\Delta$ 3d” in Tables 1–3).

### 5.8. Priors

Since the choice of priors on the various parameters is arbitrary in our analysis, it is important to determine to

what extent they could affect our conclusions. To do this, we replaced each arbitrary choice in turn with an alternative, reasonable prior. Specifically, for each parameter describing the entropy profile, we switched from a flat prior on that parameter to a flat prior on its logarithm. We used a flat prior on the DM halo mass, rather than on its logarithm, and, instead of the flat prior on  $\log c_{DM}$ , we adopted the distribution of  $c$  around  $M$  found by Buote et al. (2007) as a (Gaussian) prior. We also replaced the flat prior on the  $M_*/L_I$  ratio with a Gaussian prior, corresponding to the best-fitting  $M/L$  ratio and error-bar derived from fitting the published Lick indices (§ 6.2). For the single powerlaw mass model fits (Table 2), we used a flat prior on  $M_{75}$ , rather than its logarithm, and a flat prior on the logarithm of  $\alpha$ . The effect of these choices is comparable to the statistical errors on each derived parameter (“ $\Delta$ Fit priors” in Tables 1 and 3).

### 5.9. Other tests

We here outline the remaining tests we carried out, as summarized in Tables 1 and 3. First of all, to assess the sensitivity of our results to the choice of plasma code employed, we experimented by replacing the APEC plasma model with a MEKAL model. This had very little impact on our conclusions (“ $\Delta$ Spectral” in Tables 1–3).

In order to explore the sensitivity of our results to the entropy parameterization we adopted, we experimented with allowing an additional break at large radius. We found that the break radius was poorly constrained ( $35^{+68}_{-23}$  kpc) and adding it did not significantly improve the fit ( $\Delta\chi^2=3$  for 2 d.o.f.). Based on the ratio of the Bayesian evidence ( $6 \times 10^{-3}$ ), the model *without* the break is actually preferred at the  $\sim 2.8\text{-}\sigma$  level. Including the break had a minimal effect on the best-fitting derived parameters (“ $\Delta$ Entropy” in Tables 1–3).

In our default analysis, the projected temperature and density profile were weighted by the gas emissivity, folded through the instrumental responses (for details, see Appendix B of Gastaldello et al. 2007). Since the computation of the gas emissivity assumes that the three dimensional gas abundance profile is identical to the projected profile (which is unlikely to be true), we explored the sensitivity of our results to this approximation by adopting the extreme approach of ignoring the spatial variation of the gas emissivity altogether. We found that this had a very small effect on our results (“ $\Delta$ Weighting” in Tables 1–3).

To examine the error associated with distance uncertainties, we varied the distance to NGC 1521 by  $\pm 20\%$ , finding the effect, particularly on  $f_{\text{b}}$  and  $f_{\text{gas}}$  to be relatively minor (“ $\Delta$ Distance”). Finally, to examine the possible errors associated with our treatment of the covariance between the density data-points, we investigated adopting a more complete treatment that considers the covariance between all the temperature and density data-points, as well as adopting the more standard (but incorrect) approach of ignoring the covariance altogether. We found that this had a non-negligible, but modest impact on the derived parameters (“ $\Delta$ Covariance” in Tables 1–3).

## 6. DISCUSSION



### 6.1. The *ElIXr* Galaxy Survey

The *ElIXr* Galaxy Survey is intended, in part, to provide a sample of candidate  $L_*$  galaxies with hot gas halos which are likely to be hosted in a galaxy-scale ( $\lesssim 10^{13}M_\odot$ ) DM halo. The full sample (Buote et al. 2012) includes several objects that are known to exhibit these characteristics (e.g. NGC 720: Humphrey et al. 2011; NGC 4125: Humphrey et al. 2006; NGC 7796: O’Sullivan et al. 2007), but the majority of the galaxies have not been studied before in the X-ray. NGC 1521 was identified as an X-ray bright object, based on the short initial *ElIXr* *XMM* observation, and targeted for deep follow-up with both *Chandra* and *XMM*.

The X-ray morphology is very relaxed, without obvious disturbance and there is no bright AGN (as evinced by its modest radio emission: Condon et al. 1998, and the lack of a central X-ray point source), suggesting no evidence of jet/ gas heating in the recent past. The hot gas halo is clearly detectable out to  $\sim 200$  kpc ( $\sim 80\%$  of  $R_{500}$ , which is  $240 \pm 22$  kpc), and the temperature profile is approximately isothermal at  $kT \simeq 0.5$  keV. Despite the slightly higher mass, the properties of NGC 1521 are remarkably similar to NGC 720, making NGC 1521 one of the smallest DM halos for which interesting X-ray constraints on the mass profile have been found, and helping to populate the very sparse low-mass end of the  $c_{\text{vir}}\text{-}M_{\text{vir}}$  plane with vital new data. The properties of NGC 1521 are, in fact, very close to our expectations for *ElIXr* galaxies, providing a crucial validation of our observing strategy.

### 6.2. Hydrostatic Equilibrium

The best-fitting hydrostatic model fits the density and temperature data-points well, consistent with the gas being close to hydrostatic. Despite nontrivial temperature and density profiles that cannot be parameterized by simple models individually, a smooth, physical mass model, coupled to a monotonically rising entropy profile (i.e. that is stable against convection), was able to reproduce them well. If the gas is far from hydrostatic, this would require a remarkable conspiracy between the temperature, density and inferred mass profiles. The closeness of the system to hydrostatic is unsurprising given its relaxed X-ray morphology (§ 3).

Nevertheless, modest deviations from hydrostatic equilibrium cannot be entirely ruled out. While numerical structure formation simulations suggest that hot halos around galaxies should, indeed, be quasi-hydrostatic (e.g. Crain et al. 2010), deviations from the hydrostatic approximation may introduce systematic errors on the recovered mass of as much as  $\sim 25\%$ , if they are similar to clusters (e.g. Tsai et al. 1994; Rasia et al. 2006; Nagai et al. 2007; Piffaretti & Valdarnini 2008; Fang et al. 2009). In order to constrain such non-hydrostatic effects observationally, recent studies have begun to compare the mass distributions of galaxies inferred from stellar dynamics modelling to those independently obtained by X-rays, including several systems that are manifestly more disturbed than NGC 1521 (e.g. Humphrey et al. 2008; Churazov et al. 2008, 2010; Gebhardt & Thomas 2009; Shen & Gebhardt 2010; Das et al. 2010, 2011; Humphrey et al. 2012b). Although better control of systematic errors may be necessary before deviations from hydrostatic equilibrium can be measured accurately (e.g. Churazov

et al. 2008; Gebhardt & Thomas 2009; Das et al. 2011; Humphrey et al. 2012b), the X-ray measurements may underestimate the mass by as much as  $\sim 30\%$  in the central  $\sim 5\text{--}10$  kpc. In § 5.3, we explored plausible nonthermal pressure profiles consistent with these observations, and found that, aside from a modest increase in the total mass of the system, if nonthermal pressure at this level is present in NGC 1521, our conclusions about the global properties of the system were largely unaffected.

While subject to uncertainties in the stellar initial mass function (e.g. Treu et al. 2010; van Dokkum & Conroy 2010) and the star-formation history of the galaxy, comparisons between the stellar M/L ratio inferred from simple stellar population (SSP) models and from X-ray studies similarly suggest that deviations from hydrostatic equilibrium are generally small (Humphrey et al. 2009a). Following Humphrey et al. (2006), we estimated the stellar age ( $8.3^{+2.3}_{-1.9}$  Gyr) and metallicity ( $[Z/H]=0.30^{+0.06}_{-0.08}$ ) of NGC 1521 by fitting the models of Thomas et al. (2003) to the  $H\beta$ , Fe5270, Fe5335 and Mgb Lick indices published by Ogando et al. (2008). For a Kroupa (2001) IMF and the SSP model of Maraston (2005), this corresponds to an I-band stellar M/L ratio of  $2.6 \pm 0.6 M_\odot L_\odot^{-1}$ , which agrees well with our measurement ( $2.49^{+0.26}_{-0.42} M_\odot L_\odot^{-1}$ ). This is consistent with observations of other galaxies, and supports the idea that the hydrostatic approximation is good for NGC 1521. Nevertheless, given the uncertainties (both statistical and systematic) in this comparison, nonthermal pressure providing as much as  $\sim 40\%$  of the total support could be consistent with the data, particularly if the IMF is more bottom heavy than Kroupa; for a Salpeter IMF, for example,  $M/L=4.0 \pm 0.9$ , which is within  $\sim 2\text{-}\sigma$  of our measurement. To quantify more precisely the accuracy of the hydrostatic approximation will likely require sophisticated (orbit-based) stellar dynamical modelling of this triaxial galaxy.

### 6.3. Mass profile

Based on our hydrostatic analysis of the *Chandra* and *XMM* data, we were able to confirm the presence of dark matter in NGC 1521 at high significance ( $8.2\text{-}\sigma$ ). The constraints our model was able to place on the virial mass and concentration (Fig 8) are competitive with other X-ray determined measurements in this mass range (e.g. Humphrey et al. 2006). The system is clearly consistent both with the empirical Buote et al. (2007)  $c_{\text{vir}}\text{-}M_{\text{vir}}$  relation, and also the theoretical model of Macciò et al. (2008) (which predicts a slightly lower  $\log_{10} c_{\text{vir}} = 0.97$  at  $10^{13}M_\odot$ ). This may slightly ease tension at the low mass end between theory and observations, although more observations are needed to resolve this issue. It is expected that isolated systems have higher concentrations, on average, than the population as a whole, although the effect is not predicted to be dramatic (e.g. Macciò et al. 2008). Nevertheless, Khosroshahi et al. (2007) reported substantially enhanced concentrations in a small sample of fossil groups and isolated galaxies. While NGC 720 could be consistent with this picture, there is no evidence of such an effect in NGC 1521, and nor does the *ElIXr* galaxy NGC 4125 show such a feature (Humphrey et al. 2006). A similar conclusion was reached for the fossil groups studied by Gastaldello et al. (2007).

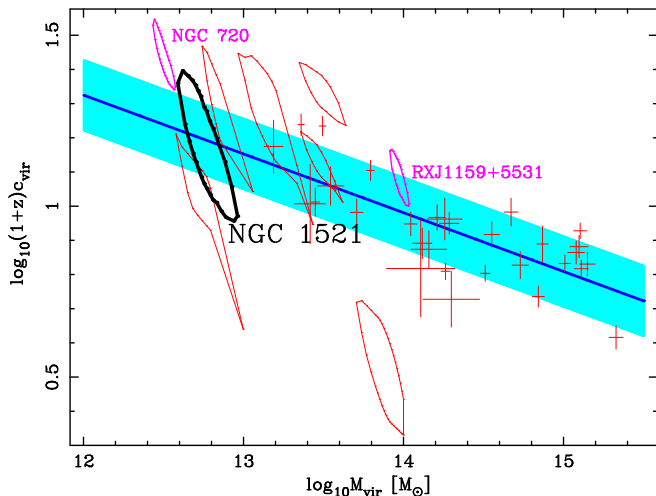


FIG. 8.— Concentration-virial mass constraints for NGC 1521, shown along with the sample of galaxies, groups and clusters in Buote et al. (2007). Where possible, we show the  $1\text{-}\sigma$  confidence contours for the objects in Humphrey et al. (2006), Humphrey et al. (2011) and Humphrey et al. (2012a). The solid blue line is the best-fitting powerlaw fit obtained by Buote et al. (2007), and the blue shaded region indicates the  $1\text{-}\sigma$  intrinsic scatter of the points about it. NGC 1521 is in good agreement with this relation.

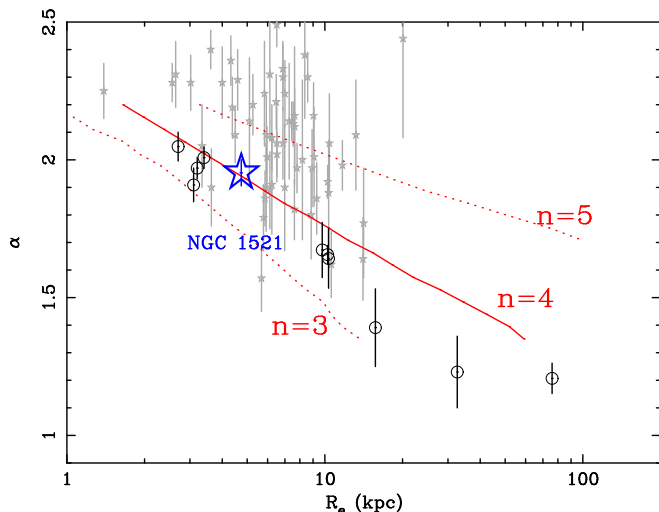


FIG. 9.— Best-fitting (total) mass slope ( $\alpha$ ) versus K-band  $R_e$  relation for NGC 1521 (blue star). We overlay (black circles) the data from Humphrey & Buote (2010), and the data derived by Auger et al. (2010) from strong lensing and stellar kinematics within  $\sim R_e$  (grey stars). The solid and dotted (red) lines are the predictions of the toy model of Humphrey & Buote (2010) for different Sérsic indices ( $n$ ) for the stellar light.

NGC 1521 is a more luminous galaxy than NGC 720 (by  $\sim 60\%$  in the K-band, and  $\sim 90\%$  in B), and so it is not surprising that it sits in a more massive halo (by a factor  $\sim 2$ ). The allowed mass range of NGC 1521 begins to approach the regime of galaxy groups ( $\gtrsim 10^{13} M_\odot$ ; Humphrey et al. 2006), but, since it represents one of the most luminous galaxies in our sample, this will likely represent the upper mass envelope of the ELIXr galaxies. While the mass constraints in NGC 1521 are competitive with the best measurements in Humphrey et al. (2006), we note that they are poorer than for NGC 720 (Humphrey et al. 2011), especially for the concentration. Although the slightly lower flux and shallower observa-

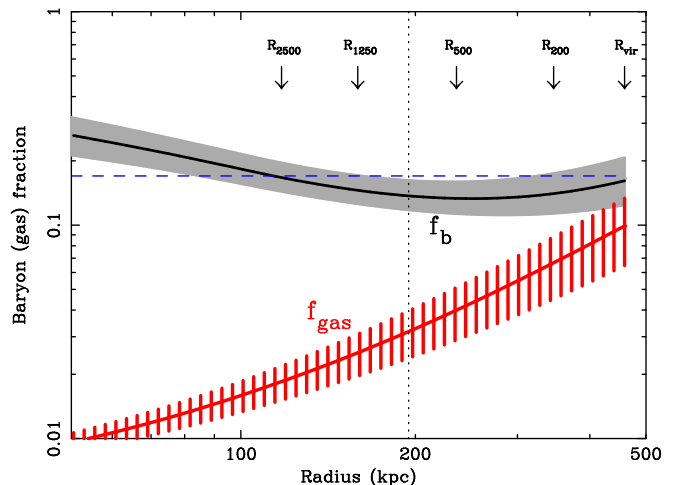


FIG. 10.— Baryon fraction profile inferred from our best-fitting models (black line). The shaded grey region indicates the  $1\text{-}\sigma$  statistical uncertainty in the fits. The red shaded region indicates the gas fraction profile and  $1\text{-}\sigma$  uncertainty. The dashed line indicates the best-fitting Cosmological value of  $f_b$ , based on the 5-year WMAP data (Dunkley et al. 2009). We indicate the physical scales corresponding to  $R_{\text{vir}}$  and various other standard radii, and the dotted line indicates the radial extent of the data being fitted. We note that the  $f_b$  profile is relatively flat, and is consistent with the Cosmic mean by  $\sim R_{\text{vir}}$ . This is very similar to the profiles measured in NGC 720 (Humphrey et al. 2011) and the fossil group RXJ1159+5531 (Humphrey et al. 2012a).

tions for NGC 1521 have some role to play in this effect, it mostly reflects degeneracies between the dark and luminous matter, since the dark matter only dominates outside  $\sim 20$  kpc, which is comparable to the scale radius ( $31_{-11}^{+19}$  kpc). Nevertheless, the virial mass is more tightly constrained, which reflects the good radial coverage at larger scales.

Even though the light profile of NGC 1521 is quite complex (§ 2.2), and so a simple interpretation in terms of the toy Sérsic+NFW model proposed by Humphrey & Buote (2010) may not be possible (i.e. the model lines in Fig 9), we found that we were able to fit the radial (total) mass distribution within  $10R_e$  with a purely powerlaw density profile distribution. In Fig 9, we show the locus of NGC 1521 in the  $\alpha$ - $R_e$  plane, which lies very close to the  $\alpha$ - $R_e$  relation established by other systems (Humphrey & Buote 2010). This further supports the idea that approximately powerlaw total mass distributions may be a natural consequence of the process of galaxy formation.

#### 6.4. Gas and baryon fraction

Based on our self-consistent hydrostatic mass model, and the fit to the density profile, we were able to constrain the gas and baryon fractions in NGC 1521, allowing a direct comparison with both NGC 720 and more massive groups and clusters. In Fig 10, we show the radial profile of  $f_{\text{gas}}$  and  $f_b$ , and we tabulate the values at various interesting scales. We see qualitatively the same behaviour as in NGC 720, i.e. an approximately flat  $f_b$  profile, close to the cosmic mean. When evaluated at  $R_{\text{vir}}$ ,  $f_b$  is consistent with baryonic closure, in agreement with the picture that the majority of the baryons exist in the hot ISM, and the behaviour seen in NGC 720 and also the more massive fossil group RXJ1159+5531 (Humphrey et al. 2012a). Within plausible systematic uncertainties, it is possible that  $f_{b,\text{vir}}$  in NGC 1521 could

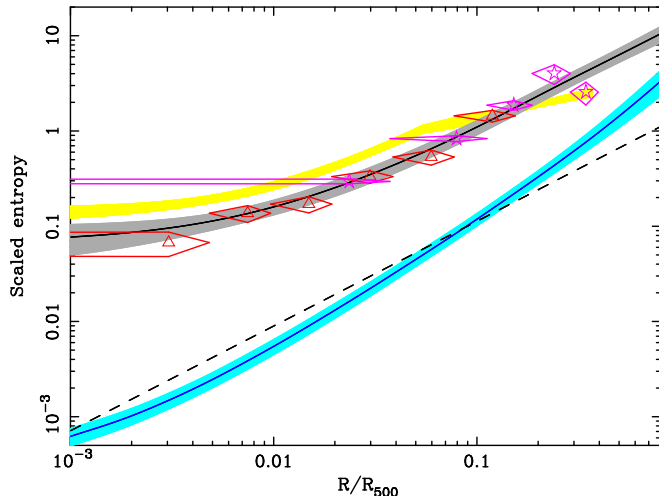


FIG. 11.—  $1\text{-}\sigma$  confidence region for the entropy profile model of NGC 1521, scaled by its characteristic entropy  $K_{500}$  ( $=38.5 \text{ keV cm}^2$ ), and shown as a function of  $R_{500}$ . We overlay deprojected entropy data-points (see § 5.7), similarly scaled. The *Chandra* data are marked with (red) triangles and the *XMM* data with (magenta) stars. The dashed line indicates the “baseline” prediction from gravitational structure formation (Voit et al. 2005). Also shown (blue shaded region) is the scaled entropy model, corrected for the gas fraction profile, which agrees better with the baseline model. In yellow we show the entropy profile for the isolated galaxy NGC 720 (Humphrey et al. 2011).

be slightly lower ( $\sim 0.10$ ), but even in that case the system has retained the bulk of its baryons. Whether the two galaxies are representative of systems at this mass-scale, or if they constitute special cases, remains to be established. Results for the full ELIXr sample will help us to address this question.

Unfortunately, the measured value of  $f_b$  in NGC 1521 does not include all of the system’s baryons. In particular, it ignores the dwarf companions, and a possible extended stellar envelope, analogous to intracluster light. Without more velocity measurements, it is difficult to estimate what fraction of the galaxies within the projected virial radius (Fig 1) should actually be included in such a calculation. Nevertheless, for a halo of  $M_{\text{vir}} = 6 \times 10^{12} M_{\odot}$ , anywhere between  $\sim 5\text{--}40\%$  of the total stellar light could be in the satellite galaxies and extended envelope (Purcell et al. 2007; Gonzalez et al. 2007), which could lead to an underestimate in  $f_{b,\text{vir}}$  of at most  $\sim 0.04$ , which is comparable to the statistical errors. We note that NGC 1521 itself does not contain significant cool gas (Huchtmeier 1994).

In contrast,  $f_{\text{gas}}$  is more robustly known, and can easily be compared to measurements in other systems. Within  $R_{500}$ , we found that  $f_{\text{gas}}$  is in good agreement with an extrapolation of the trends seen in galaxy groups and clusters; extrapolating the  $f_{\text{gas}}\text{-}R_{500}$  relation from Gioldini et al. (2009) to the mass of NGC 1521, we would expect  $f_{\text{gas}} = 0.046 \pm 0.008$ , very close to the observed value  $0.040^{+0.006}_{-0.008}$ . Similar behaviour was seen in NGC 720 (Humphrey et al. 2011).

### 6.5. Entropy profile

As expected for approximately hydrostatic gas, we find that we obtain a good fit to the data with a model requiring a monotonically rising entropy ( $S$ ) profile. We show the model profile in Fig 11 (grey shaded region),

scaled by the “characteristic entropy”  $K_{500}$ , and shown as a function of fraction of  $R_{500}$  reached. We find that the characteristic shape of the profile is qualitatively similar to that of NGC 720, showing a central “plateau”, and gradual steepening of the profile with radius, approximately reaching  $S \propto R^{1.1}$ , although it does not exhibit the flattening outside  $\sim 0.1R_{500}$  in that galaxy. At all radii, the entropy profile is significantly enhanced over the “baseline” model for gravity-only structure formation simulations (Voit et al. 2005), indicating significant entropy injection. Given the more massive halo of NGC 1521, as compared to NGC 720, it is unsurprising that the entropy injection appears to have affected the profile more significantly in the latter.

To provide a less model-dependent view of the entropy profile, we overlay in Fig 11 a series of data-points, which are directly computed from the deprojected density and temperature profiles. These were obtained by emulating the behaviour of the “*projct*” *Xspec* model, and correcting for emission projected into the line of sight from outside the outermost annulus (see § 5.7). These data agree well with the smooth model, giving us confidence in our projection procedure.

Following Pratt et al. (2010), we investigated whether scaling the entropy profile by a correction factor  $((f_g(R)/f_{b,U})^{2/3})$ , where  $f_g(R)$  is the gas fraction profile, and  $f_{b,U}$  is the Cosmic baryon fraction, 0.17) brings it into better agreement with the baseline model. We show this “ $f_{\text{gas}}$ -corrected” entropy profile in Fig 11, which clearly agrees much better with the baseline model. This is consistent with a picture in which entropy injection primarily manifests itself by pushing the gas out to large radii.

### 6.6. Abundance profile

An intriguing result from our study is the detection of a negative abundance gradient in the hot ISM of NGC 1521 (Fig 5), very similar to trends seen in relaxed galaxy groups (e.g. Humphrey & Buote 2006; Buote 2002; Buote et al. 2003, 2004; Rasmussen & Ponman 2007), and the  $\sim$ Milky Way-mass elliptical NGC 720 (Humphrey et al. 2011). This suggests that such abundance gradients may be commonplace even in isolated (X-ray bright) elliptical galaxies, which has implications for the bulk gas motions responsible for distributing the metals (Mathews & Brighenti 2003), and may imply large-scale flows driven by low-level AGN heating (Mathews et al. 2004).

In general, the emission-weighted Fe abundance ( $Z_{\text{Fe}}$ ) of the hot ISM in an early-type galaxy is consistent with, or higher than, the metallicity of the stars (Humphrey & Buote 2006). In the case of NGC 1521, however, there appears some tension between the two measurements; using *XMM*, the Fe abundance, even averaged over the central  $\sim 10$  kpc is only  $0.44 \pm 0.09$  times Solar, while the results from fitting the published Lick indices (see § 6.2; Ogando et al. 2008) imply a global stellar abundance of  $1.4 \pm 0.3$  times Solar, making this system an outlier ( $\sim 3.6\text{-}\sigma$  away from equality between the metallicity of the stars and gas) from the relation found by Humphrey & Buote (2006). One possible solution to this problem is the “Fe bias”, a systematic underestimate of the Fe abundance when a single temperature plasma model is fitted to an inherently multi-temperature X-ray spectrum (Buote &

Fabian 1998; Buote 2000b). Although the temperature profile of NGC 1521 is close to isothermal, we experimented with adding an additional  $\sim 0.2$  keV gas component to the central *XMM* bin. The fit improved modestly ( $\Delta C=9.7$  for 2 degrees of freedom), with  $\sim 30\%$  of the gas in that bin in the cooler phase, and we found a subtle increase in the best-fitting abundance, accompanied by a significantly expanded error bar ( $Z_{\text{Fe}}=0.50^{+0.22}_{-0.08}$ ). The increase of the error bar slightly eased tension with the other objects discussed in Humphrey & Buote (2006), making it only  $\sim 2.7\text{-}\sigma$  discrepant with parity between the metallicities of the gas and stars. We note that, although this would suggest non-isothermal gas in the central region, one can still obtain reliable mass profiles with our modelling procedure by interpreting a single-temperature fit to the data, provided care is taken to average the model suitably, as we did in the present work (Gastaldello et al. 2007).

We would like to thank Aaron Barth and Luis

Ho for kindly providing their optical data, taken as part of the Carnegie-Irvine Galaxy Survey (<http://cgs.obs.carnegiescience.edu/CGS/Home.html>). We would also like to thank Fabio Gastaldello for discussions and support with the *XMM* analysis. We thank Christina Topchyan for suggesting the acronym EIIXr. This research made use of the NASA/IPAC Extragalactic Database (*NED*) which is operated by the Jet Propulsion Laboratory, California Institute of Technology, under contract with NASA, and the HyperLEDA database (<http://leda.univ-lyon1.fr>). We are grateful to the WIND-SWE team for making their data publicly available. PJH and DAB gratefully acknowledge support from *Chandra* award G09-0092X, issued by the *Chandra* X-ray Center, which is operated by the Smithsonian Astrophysical Observatory for and on behalf of NASA. Partial support for this work was also provided by NASA under *XMM* grant NNX08AX74G and grant NNX10AD07G, issued through the office of Space Science Astrophysics Data Program.

#### REFERENCES

- Abadi, M. G., Navarro, J. F., Fardal, M., Babul, A., & Steinmetz, M. 2010, *MNRAS*, 407, 435
- Anderson, M. E. & Bregman, J. N. 2010, *ApJ*, 714, 320
- Anderson, M. E. & Bregman, J. N. 2011, *ApJ*, 737, 22
- Asplund, M., Grevesse, N., & Sauval, J. 2004, in *Cosmic abundances as records of stellar evolution and nucleosynthesis*, ed. F. N. Bash & T. G. Barnes (ASP Conf. series), astro-ph/0410214
- Auger, M. W., Treu, T., Bolton, A. S., Gavazzi, R., Koopmans, L. V. E., Marshall, P. J., Moustakas, L. A., & Burles, S. 2010, *ApJ*, 724, 511
- Benson, A. J., Bower, R. G., Frenk, C. S., Lacey, C. G., Baugh, C. M., & Cole, S. 2003, *ApJ*, 599, 38
- Benson, A. J., Bower, R. G., Frenk, C. S., & White, S. D. M. 2000, *MNRAS*, 314, 557
- Binney, J. 1985, *MNRAS*, 212, 767
- Binney, J. & Tremaine, S. 2008, *Galactic Dynamics* (2<sup>nd</sup> ed.; Princeton, NJ: Princeton University Press)
- Blumenthal, G. R., Faber, S. M., Flores, R., & Primack, J. R. 1986, *ApJ*, 301, 27
- Bregman, J. N. & Lloyd-Davies, E. J. 2007, *ApJ*, 669, 990
- Bryan, G. L. & Norman, M. L. 1998, *ApJ*, 495, 80
- Bullock, J. S., Kolatt, T. S., Sigad, Y., Somerville, R. S., Kravtsov, A. V., Klypin, A. A., Primack, J. R., & Dekel, A. 2001, *MNRAS*, 321, 559
- Buote, D. A. 2000a, *ApJ*, 539, 172
- Buote, D. A. 2000b, *MNRAS*, 311, 176
- Buote, D. A. 2002, *ApJ*, 574, L135
- Buote, D. A., Brighenti, F., & Mathews, W. G. 2004, *ApJ*, 607, L91
- Buote, D. A. & Fabian, A. C. 1998, *MNRAS*, 296, 977
- Buote, D. A., Gastaldello, F., Humphrey, P. J., Zappacosta, L., Bullock, J. S., Brighenti, F., & Mathews, W. G. 2007, *ApJ*, 664, 123
- Buote, D. A. & Humphrey, P. J. 2012a, in *Astrophysics and Space Science Library*, Vol. 378, *Astrophysics and Space Science Library*, ed. D.-W. Kim & S. Pellegrini, 235
- Buote, D. A. & Humphrey, P. J. 2012b, *MNRAS*, 420, 1693
- Buote, D. A. & Humphrey, P. J. 2012c, *MNRAS*, 421, 1399
- Buote, D. A., Lewis, A. D., Brighenti, F., & Mathews, W. G. 2003, *ApJ*, 595, 151
- Buote, D. A. & Tsai, J. C. 1995, *ApJ*, 439, 29
- Buote, D. A., Zappacosta, L., Fang, T., Humphrey, P. J., Gastaldello, F., & Tagliaferri, G. 2009, *ApJ*, 695, 1351
- Buote, D. A. et al. 2012, in preparation
- Canizares, C. R., Fabbiano, G., & Trinchieri, G. 1987, *ApJ*, 312, 503
- Capaccioli, M., Pionto, G., & Rampazzo, R. 1988, *AJ*, 96, 487
- Cappellari, M. 2002, *MNRAS*, 333, 400
- Churazov, E., Forman, W., Vikhlinin, A., Tremaine, S., Gerhard, O., & Jones, C. 2008, *MNRAS*, 388, 1062
- Churazov, E., Tremaine, S., Forman, W., Gerhard, O., Das, P., Vikhlinin, A., Jones, C., Böhringer, H., & Gebhardt, K. 2010, *MNRAS*, 359
- Condon, J. J., Cotton, W. D., Greisen, E. W., Yin, Q. F., Perley, R. A., Taylor, G. B., & Broderick, J. J. 1998, *AJ*, 115, 1693
- Crain, R. A., McCarthy, I. G., Frenk, C. S., Theuns, T., & Schaye, J. 2010, *MNRAS*, 407, 1403
- Croton, D. J., Springel, V., White, S. D. M., De Lucia, G., Frenk, C. S., Gao, L., Jenkins, A., Kauffmann, G., Navarro, J. F., & Yoshida, N. 2006, *MNRAS*, 365, 11
- Das, P., Gerhard, O., Churazov, E., & Zhuravleva, I. 2010, *MNRAS*, 409, 1362
- Das, P., Gerhard, O., Mendez, R. H., Teodorescu, A. M., & de Lorenzi, F. 2011, *MNRAS*, 415, 1244
- de Lorenzi, F., et al. 2009, *MNRAS*, 395, 76
- De Luca, A. & Molendi, S. 2004, *A&A*, 419, 837
- Dekel, A. & Silk, J. 1986, *ApJ*, 303, 39
- Duffy, A. R., Schaye, J., Kay, S. T., Dalla Vecchia, C., Battye, R. A., & Booth, C. M. 2010, *MNRAS*, 405, 2161
- Dunkley, J., et al. 2009, *ApJS*, 180, 306
- Ellis, S. C. & O'Sullivan, E. 2006, *MNRAS*, 367, 627
- Faber, S. M., Wegner, G., Burstein, D., Davies, R. L., Dressler, A., Lynden-Bell, D., & Terlevich, R. J. 1989, *ApJS*, 69, 763
- Fang, T., Buote, D. A., Humphrey, P. J., Canizares, C. R., Zappacosta, L., Maiolino, R., Tagliaferri, G., & Gastaldello, F. 2010, *ApJ*, 714, 1715
- Fang, T., Humphrey, P., & Buote, D. 2009, *ApJ*, 691, 1648
- Fang, T., Marshall, H. L., Lee, J. C., Davis, D. S., & Canizares, C. R. 2002, *ApJ*, 572, L127
- Fang, T., Mckee, C. F., Canizares, C. R., & Wolfire, M. 2006, *ApJ*, 644, 174
- Feroz, F., Hobson, M. P., & Bridges, M. 2009, *MNRAS*, 398, 1601
- Finoguenov, A. & Ponman, T. J. 1999, *MNRAS*, 305, 325
- Fukazawa, Y., Botoya-Nonesu, J. G., Pu, J., Ohto, A., & Kawano, N. 2006, *ApJ*, 636, 698
- Fukugita, M., Hogan, C. J., & Peebles, P. J. E. 1998, *ApJ*, 503, 518
- Fukugita, M. & Peebles, P. J. E. 2006, *ApJ*, 639, 590
- Gastaldello, F., Buote, D. A., Humphrey, P. J., Zappacosta, L., Bullock, J. S., Brighenti, F., & Mathews, W. G. 2007, *ApJ*, 669, 158
- Gavazzi, R., Treu, T., Rhodes, J. D., Koopmans, L. V. E., Bolton, A. S., Burles, S., Massey, R. J., & Moustakas, L. A. 2007, *ApJ*, 667, 176
- Gebhardt, K. & Thomas, J. 2009, *ApJ*, 700, 1690
- Giodini, S., et al. 2009, *ApJ*, 703, 982

- Gnedin, O. Y., Kravtsov, A. V., Klypin, A. A., & Nagai, D. 2004, *ApJ*, 616, 16
- Gnedin, O. Y., Weinberg, D. H., Pizagno, J., Prada, F., & Rix, H.-W. 2007, *ApJ*, 671, 1115
- Gonzalez, A. H., Zaritsky, D., & Zabludoff, A. I. 2007, *ApJ*, 666, 147
- Gültekin, K., et al. 2009, *ApJ*, 698, 198
- Helsdon, S. F., Ponman, T. J., O'Sullivan, E., & Forbes, D. A. 2001, *MNRAS*, 325, 693
- Henley, D. B., Shelton, R. L., Kwak, K., Joung, M. R., & Mac Low, M.-M. 2010, *ApJ*, 723, 935
- Ho, L. C., Li, Z.-Y., Barth, A. J., Seigar, M. S., & Peng, C. Y. 2011, *ApJS*, 197, 21
- Hopkins, P. F., Hernquist, L., Cox, T. J., Di Matteo, T., Robertson, B., & Springel, V. 2006, *ApJS*, 163, 1
- Huchtmeier, W. K. 1994, *A&A*, 286, 389
- Humphrey, P. J. & Buote, D. A. 2006, *ApJ*, 639, 136
- Humphrey, P. J. & Buote, D. A. 2010, *MNRAS*, 403, 2143
- Humphrey, P. J., Buote, D. A., Brighenti, F., Flohic, H. M. L. G., Gastaldello, F., & Mathews, W. G. 2012a, *ApJ*, 748, 11
- Humphrey, P. J., Buote, D. A., Brighenti, F., Gebhardt, K., & Mathews, W. G. 2008, *ApJ*, 683, 161
- Humphrey, P. J., Buote, D. A., Brighenti, F., Gebhardt, K., & Mathews, W. G. 2009a, *ApJ*, 703, 1257
- Humphrey, P. J., Buote, D. A., Brighenti, F., Gebhardt, K., & Mathews, W. G. 2012b, in prep.
- Humphrey, P. J., Buote, D. A., Canizares, C. R., Fabian, A. C., & Miller, J. M. 2011, *ApJ*, 729, 53
- Humphrey, P. J., Buote, D. A., Gastaldello, F., Zappacosta, L., Bullock, J. S., Brighenti, F., & Mathews, W. G. 2006, *ApJ*, 646, 899
- Humphrey, P. J., Liu, W., & Buote, D. A. 2009b, *ApJ*, 693, 822
- Jarrett, T. H. 2000, *PASP*, 112, 1008
- Kalberla, P. M. W., Burton, W. B., Hartmann, D., Arnal, E. M., Bajaja, E., Morras, R., & Pöppel, W. G. L. 2005, *A&A*, 440, 775
- Kaufmann, T., Bullock, J. S., Maller, A. H., Fang, T., & Wadsley, J. 2009, *MNRAS*, 396, 191
- Kereš, D., Katz, N., Weinberg, D. H., & Davé, R. 2005, *MNRAS*, 363, 2
- Khosroshahi, H. G., Ponman, T. J., & Jones, L. R. 2007, *MNRAS*, 377, 595
- Klypin, A., Zhao, H., & Somerville, R. S. 2002, *ApJ*, 573, 597
- Koopmans, L. V. E., Bolton, A., Treu, T., Czoske, O., Auger, M. W., Barnabè, M., Vegetti, S., Gavazzi, R., Moustakas, L. A., & Burles, S. 2009, *ApJ*, 703, L51
- Kriss, G. A., Cioffi, D. F., & Canizares, C. R. 1983, *ApJ*, 272, 439
- Kroupa, P. 2001, *MNRAS*, 322, 231
- Kuntz, K. D. & Snowden, S. L. 2000, *ApJ*, 543, 195
- Kuntz, K. D. & Snowden, S. L. 2008, *A&A*, 478, 575
- Li, Z.-Y., Ho, L. C., Barth, A. J., & Peng, C. Y. 2011, *ApJS*, 197, 22
- Macciò, A. V., Dutton, A. A., & van den Bosch, F. C. 2008, *MNRAS*, 391, 1940
- Maller, A. H. & Bullock, J. S. 2004, *MNRAS*, 355, 694
- Mandelbaum, R., Seljak, U., Cool, R. J., Blanton, M., Hirata, C. M., & Brinkmann, J. 2006, *MNRAS*, 372, 758
- Maraston, C. 2005, *MNRAS*, 362, 799
- Mathews, W. G. & Brighenti, F. 2003, *ARA&A*, 41, 191
- Mathews, W. G., Brighenti, F., & Buote, D. A. 2004, *ApJ*, 615, 662
- Mathews, W. G., Brighenti, F., Faltenbacher, A., Buote, D. A., Humphrey, P. J., Gastaldello, F., & Zappacosta, L. 2006, *ApJ*, 652, L17
- McGaugh, S. S., Schombert, J. M., de Blok, W. J. G., & Zagursky, M. J. 2010, *ApJ*, 708, L14
- Memola, E., Salucci, P., & Babić, A. 2011, *A&A*, 534, A50+
- Nagai, D., Vikhlinin, A., & Kravtsov, A. V. 2007, *ApJ*, 655, 98
- Naranan, S., Shulman, S., Friedman, H., & Fritz, G. 1976, *ApJ*, 208, 718
- Navarro, J. F., Frenk, C. S., & White, S. D. M. 1997, *ApJ*, 490, 493
- Navarro, J. F., Hayashi, E., Power, C., Jenkins, A. R., Frenk, C. S., White, S. D. M., Springel, V., Stadel, J., & Quinn, T. R. 2004, *MNRAS*, 349, 1039
- Nicastro, F., Zezas, A., Drake, J., Elvis, M., Fiore, F., Fruscione, A., Marengo, M., Mathur, S., & Bianchi, S. 2002, *ApJ*, 573, 157
- Nomoto, K., Hashimoto, M., & Tsujimoto, T. 1997a, *Nucl. Phys. A*, 616, 79
- Nomoto, K., Iwamoto, K., Nakasoto, N., Thielemann, F. K., Brachwitz, F., Tsujimoto, T., Kubo, Y., & Kishimoto, N. 1997b, *Nucl. Phys. A*, 621, 467
- Ogando, R. L. C., Maia, M. A. G., Pellegrini, P. S., & da Costa, L. N. 2008, *AJ*, 135, 2424
- Ogilvie, K. W., et al. 1995, *Space Sci. Rev.*, 71, 55
- Oppenheimer, B. D. & Davé, R. 2006, *MNRAS*, 373, 1265
- O'Sullivan, E., Forbes, D. A., & Ponman, T. J. 2001, *MNRAS*, 328, 461
- O'Sullivan, E. & Ponman, T. J. 2004, *MNRAS*, 354, 935
- O'Sullivan, E., Sanderson, A. J. R., & Ponman, T. J. 2007, *MNRAS*, 380, 1409
- Piffaretti, R. & Valdarnini, R. 2008, *A&A*, 491, 71
- Pratt, G. W., Arnaud, M., Piffaretti, R., Böhringer, H., Ponman, T. J., Croston, J. H., Voit, G. M., Borgani, S., & Bower, R. G. 2010, *A&A*, 511, A85+
- Prugniel, P. & Simien, F. 1997, *A&A*, 321, 111
- Purcell, C. W., Bullock, J. S., & Zentner, A. R. 2007, *ApJ*, 666, 20
- Ramella, M., Geller, M. J., Pisani, A., & da Costa, L. N. 2002, *AJ*, 123, 2976
- Rasia, E., Ettori, S., Moscardini, L., Mazzotta, P., Borgani, S., Dolag, K., Tormen, G., Cheng, L. M., & Diaferio, A. 2006, *MNRAS*, 369, 2013
- Rasmussen, A., Kahn, S. M., & Paerels, F. 2003, in *Astrophysics and Space Science Library*, Vol. 281, *The IGM/Galaxy Connection. The Distribution of Baryons at z=0*, ed. J. L. Rosenberg & M. E. Putman, 109+
- Rasmussen, J. & Ponman, T. J. 2007, *MNRAS*, 380, 1554
- Rasmussen, J., Sommer-Larsen, J., Pedersen, K., Toft, S., Benson, A., Bower, R. G., & Grove, L. F. 2009, *ApJ*, 697, 79
- Schlegel, D. J., Finkbeiner, D. P., & Davis, M. 1998, *ApJ*, 500, 525
- Schweizer, F. & Seitzer, P. 1992, *AJ*, 104, 1039
- Shen, J. & Gebhardt, K. 2010, *ApJ*, 711, 484
- Snowden, S. L., Burrows, D. N., Sanders, W. T., Aschenbach, B., & Pfeiffermann, E. 1995, *ApJ*, 439, 399
- Snowden, S. L., Collier, M. R., & Kuntz, K. D. 2004, *ApJ*, 610, 1182
- Snowden, S. L., Egger, R., Freyberg, M. J., McCammon, D., Plucinsky, P. P., Sanders, W. T., Schmitt, J. H. M. M., Truemper, J., & Voges, W. 1997, *ApJ*, 485, 125
- Snowden, S. L., Mushotzky, R. F., Kuntz, K. D., & Davis, D. S. 2008, *A&A*, 478, 615
- Sun, M., Voit, G. M., Donahue, M., Jones, C., Forman, W., & Vikhlinin, A. 2009, *ApJ*, 693, 1142
- Thomas, D., Maraston, C., & Bender, R. 2003, *MNRAS*, 339, 897
- Thomas, J., Jesseit, R., Naab, T., Saglia, R. P., Burkert, A., & Bender, R. 2007, *MNRAS*, 381, 1672
- Treu, T., Auger, M. W., Koopmans, L. V. E., Gavazzi, R., Marshall, P. J., & Bolton, A. S. 2010, *ApJ*, 709, 1195
- Tsai, J. C., Katz, N., & Bertschinger, E. 1994, *ApJ*, 423, 553
- van Dokkum, P. G. & Conroy, C. 2010, *Nature*, 468, 940
- Voit, G. M., Kay, S. T., & Bryan, G. L. 2005, *MNRAS*, 364, 909
- White, S. D. M. & Frenk, C. S. 1991, *ApJ*, 379, 52
- White, S. D. M. & Rees, M. J. 1978, *MNRAS*, 183, 341